Ollscoil
Mhá Nuad
Ollscoil na hÉireann
Má Nuad

Dynamics of the Gross-Pitaevskii Equation and Shortcuts to Adiabaticity

Shane Short B.Sc.

A thesis submitted for the degree of

Masters by Research

to the

Department of Theoretical Physics

Maynooth University

Department Head: Prof. Peter Coles

Supervisor: Dr. Masudul Haque

June, 2021

Acknowledgements

Throughout the writing of this thesis I have received help and advice from a great number of people.

I would first like to thank my supervisor, Dr Masudul Haque, without whom, this research would never have been undertaken.

I would like to thank my colleagues from the department of Theoretical Physics in Maynooth. Phillip C. Burke and Adam Tallon with whom I was lucky enough to share an office space. Aonghus Hunter McCabe, and Dale Lawlor who kept me sane during the final months of writing and also helped with proof reading. I would also be amiss not to thank Nathan Keenan and Goran Nakerst for countless helpful discussions over the course of this research.

Finally, and most importantly, I would like to thank my family for their help over the years of my education to this point. Without the support of my mother Geraldine, my father Matt, and my sister Niamh, I would have undoubtedly faltered many years ago.

Dynamics of the Gross-Pitaevskii Equation and Shortcuts to Adiabaticity

Abstract

Procedures which vary the parameters of a model in an adiabatic way have applications in many areas of quantum technology. However, explicitly employing adiabatic evolution often leads to decoherence issues due to systems interacting with their environment. For this reason, there has been much interest in developing *shortcuts to adiabaticity* in which the target final state is reached in a finite duration change of parameter. In this thesis, we design and study a shortcut to adiabaticity in an interacting Bose-Einstein condensate. In particular, we study the response induced by ramps in the interaction strength of such a system. We determine the power law decay exponents of the induced excitations as well as the characteristic frequency with which these excitations oscillate with respect to the duration and mean values of the ramps.

Chapter 1

Introduction

In this thesis, we study the dynamics of a Bose-Einstein condensate modelled by the Gross-Pitaevskii equation and methods of shortcuts to adiabaticity in these systems. In this introductory chapter we initially provide some background discussion regarding Bose-Einstein condensation and the Gross-Pitaevskii equation in section 1.1. We then introduce the need for methods referred to as shortcuts to adiabaticity and discuss some of the current literature surrounding this area of study in section 1.2. Finally in section 1.3 we give an overview of the composition of the entire thesis.

1.1 Background material for Bose-Einstein condensation

In quantum mechanics, in particular quantum statistics, particles are divided into two classes, Bosons and Fermions. The statistics of how members of these classes interact in large numbers have many far-reaching consequences in all areas of physics. For example, the entire structure of the periodic table

arises from the behaviour of two Fermions under exchange. Arguably, the most dramatic consequence of these quantum statistics is the phenomenon of Bose-Einstein condensation (BEC). This exotic state of matter was first predicted by Albert Einstein and Satyendra Nath Bose in 1924. The first experimental realisation of such a material was by teams in the University of Colorado and MIT in 1995. In the decades since these initial experiments, BEC systems have been an area of intense theoretical and experimental research.

This section will be split into four main subsections. In 1.1.1 we briefly discuss the notion of indistinguishable particles and the implications of this idea. In 1.1.2 and 1.1.3 we outline the behaviour of systems of Bosons leading to a BEC. Finally, in 1.1.4 we discuss the Gross-Pitaevskii equation (GPE), its appearances in the literature, and some analytic and numerical methods used in solving it.

1.1.1 Indistinguishable particles and the Pauli exclusion principle

The wealth of physics that arise from these exchange statistics can be traced back to two important concepts: the Pauli exclusion principle (and the spin statistics theorem which follows), and the indistinguishability of particles in quantum systems. To begin with, here we briefly discuss what it means for a pair of particles to be indistinguishable.

In the classical world if we wanted to tell two particles apart, we could do so by measuring their physical properties such as mass or charge. However, we know that in the subatomic world two electrons will share the same mass, two protons will have the same charge, and so on. This means measuring the qualities of the particles cannot help us in distinguishing them. We might

then try to follow their paths from point A to point B, like following a ball under a cup, to tell them apart at their final destination. In the classical limit of quantum mechanics, ie. the limit of sufficiently high temperatures or similarly low particle density, this approach may be feasible. In a quantum system however, as the mean separation between particles approaches the de Broglie wavelength of said particles it would become impossible to distinguish particles in this manner.

In a quantum system this analagous description can be defined as an invariance of multiparticle systems up to some global phase with respect to an interchange of particles. In a system composed of both Bosons and Fermions this phase invariance holds independently for either class of particle.

In such a quantum system then, we may consider the phase picked up by a two particle exchange to be

$$\psi \to \psi e^{i\theta} \tag{1.1}$$

, where the angle θ is determined by the type of particle. Regardless of the type of particle, if we performed this exchange twice, we would expect to return to the initial state meaning

$$e^{2i\theta} = 1. \tag{1.2}$$

This implies that for a single exchange the available phases are either $+1$ or -1 corresponding to Bosons and Fermions respectively. By considering the behaviour of two particle exchanges in this manner we arrive at the essential ingredient for Bose-Einstein condensation: the Pauli exclusion principle. For Fermions this exclusion principle means the probability of two Fermions occupying the same state is necessarily zero. Conversely, as Bosons do not obey this principle, there is no mechanism preventing any number of Bosons from occupying the same quantum state.

The Pauli exclusion principle explains a wide range of phenomena in physics. For Fermions, the structure imposed by this condition gives rise to the periodic table, electron degeneracy in white dwarves and even the simple notion of atoms occupying space.

The inapplicability of this principle to Bosons also allows some peculiar behaviour to occur in many body systems of Bosons. For example, coherent photons are used to create laser light via the mechanism of population inversion[1]. However, the most relevant implication for this thesis is the abrupt accumulation of atoms in the ground state of the system below some critical temperature known as Bose-Einstein condensation (BEC).

A discussion of the characteristics of BEC can be found in any condensed matter or statistical mechanics textbooks. Here we provide a short summary of the main points. In particular, we discuss the bias towards ground state occupation in systems of bosons compared to the classical treatment of particles in 1.1.2. We then make some approximate calculations of the temperature ranges involved in Bose-Einstein condensation in 1.1.3. A more detailed discussion of these accounts can be found in [1].

1.1.2 Ground state occupation in systems of Bosons

In the previous section, we discussed the Pauli exclusion principle and the implications of it for symmetric and antisymmetric particles. These exchange statistics when considered in conjunction with the canonical partition function lead to the following statistical distributions for Bosons and Fermions

[1]The term population inversion describes a system of atoms in which the majority exist in an excited state rather than the ground state

respectively:

$$\langle n^{BE} \rangle = \frac{1}{e^{\beta(\epsilon-\mu)} - 1} \quad , \quad \langle n^{FD} \rangle = \frac{1}{e^{\beta(\epsilon-\mu)} + 1} \tag{1.3}$$

, where μ is the chemical potential and $\beta = \frac{1}{k_B T}$ is the inverse temperature. We refer to the Bose-Einstein and Fermi-Dirac distributions as n_{BE} and n_{FD} respectively. In either case here $\langle n \rangle$ gives the expected number of particles with energy ϵ. For the purposes of comparison, we also mention the Maxwell-Boltzmann distribution n_{MB}

$$\langle n^{MB} \rangle = \frac{1}{e^{\beta(\epsilon-\mu)}}. \tag{1.4}$$

The Maxwell-Boltzmann distribution describes systems of distinguishable particles. Despite (1.4) being entirely unphysical as no real particles display these statistics it is still useful to consider as a high temperature limit of n_{BE} and n_{FD}.

As an illustrative example of Bose-Einstein condensation, here we consider a system of free Bosons in a cube of length L. We study how the system responds to changes in temperature when treated using Bose-Einstein and Maxwell-Boltzmann statistics.

By setting the ground state energy $\epsilon_0 = 0$ (which we can do without loss of generality) we can write the number of Bosons in the lowest energy state N_0 as

$$N_0 = \frac{1}{e^{-\beta\mu} - 1}. \tag{1.5}$$

Similarly the total number of Bosons in the whole system is given by the sum over all available states

$$N = \sum_n \frac{1}{e^{\beta(\epsilon_n-\mu)} - 1} = \sum_n \frac{1}{e^{\beta\epsilon_n} e^{-\beta\mu} - 1}. \tag{1.6}$$

If we solve (1.5) for $e^{-\beta\mu}$ we can write the total atom number in terms of the energy eigenvalues and the ground state occupation

$$N = \sum_n \frac{1}{e^{\beta\epsilon_n}\left(\frac{1}{N_0}+1\right)-1}. \tag{1.7}$$

The energy of a free Boson in a cube can be found by considering the free particle Schrödinger equation for particles with momentum $k^2 = \frac{2m\epsilon}{\hbar^2}$.

$$\nabla^2\psi(x) + k^2\psi(x) = 0. \tag{1.8}$$

The general solution of this ODE is $\psi(x) = A\sin(kx) + B\cos(kx)$. Imposing Dirichlet boundary conditions at the edges of the cube gives us momenta $k = \frac{n\pi}{L}$ and thus energies

$$\epsilon_n = \frac{\hbar^2\pi^2}{2mL^2}n^2 = \epsilon_1 n^2. \tag{1.9}$$

By inserting this expression of the system energies into equation (1.7) we find the total atom number in terms of the energy of the first excited state, the temperature of the system, and the ground state occupation

$$N = \sum_{n_x,n_y,n_z=0} \frac{1}{e^{\beta\epsilon_1\left(n_x^2+n_y^2+n_z^2\right)}\left(\frac{1}{N_0}+1\right)-1}. \tag{1.10}$$

We would like to invert this expression in order to express the ground state occupation in terms of the total atom number N and temperature T. Of course, this involves computing the sum above, which is not possible. Performing the sum numerically[2] however is sufficient for this illustrative example. Additionally, for the purposes of comparison, the same calculation for the Maxwell-Boltzmann statistics leads to ground state occupancy

$$N = N_0 \sum_{n_x,n_y,n_z=0} e^{-\beta\epsilon_1\left(n_x^2+n_y^2+n_z^2\right)}. \tag{1.11}$$

[2]Sum is calculated up to the $n_x = n_y = n_z = 16$ energy level.

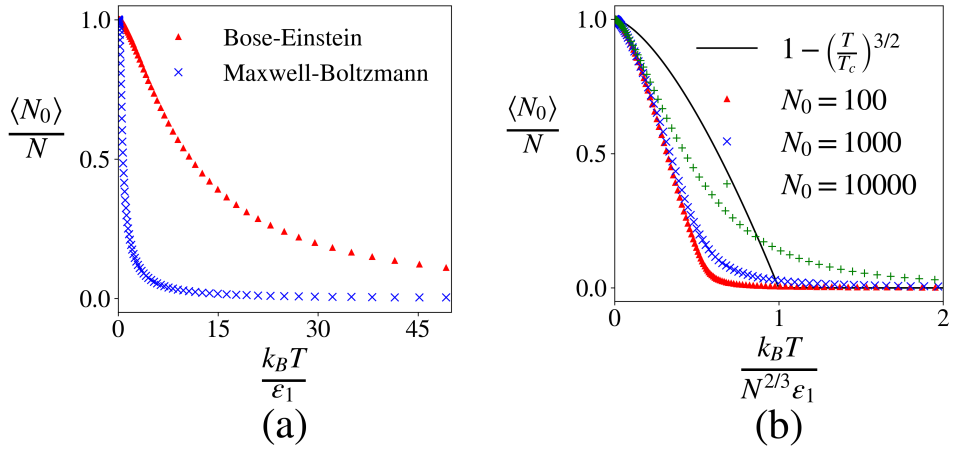

Figure 1.1: **(a)** Relative ground state occupation of particles in a cube using equation (1.10) n_{BE} statistics and equation (1.11) n_{MB} distributions. **(b)** Relative ground state occupation of Bosons calculated numerically from equations (1.10) and (1.11) and rescaled by $N^{-2/3}$ as discussed after equation (1.18) compared to the analytic result equation (1.18).

In figure 1.1 **(a)** the particles following Bose-Einstein statistics display the overwhelming preference towards occupying the ground state known as Bose condensation. Even at relatively high temperatures N_0^{BE} is several orders of magnitude larger than the classical Boltzmann analogue.

This feature of Bose gases was predicted in 1925 early in the development of the then new field of quantum statistics. First, by Satyendra Nath Bose for photons and then extended to all Bosons by Albert Einstein. Many technologies were to be developed before Bose Condensation would be realised experimentally. In the following section we continue this analysis of the Bose-Einstein distribution with the intention of approximating the temperature ranges typical in Bose-Einstein condensates.

1.1.3 Critical temperatures

In the previous section, we showed that systems of Bosons tend to accumulate in the ground state as a result of Bose-Einstein statistics. This macroscopic occupation occurs at temperatures significantly higher than those predicted by the classical Maxwell-Bolzmann statistics, however the necessary temperatures are still extremely low. Here we discuss just how low a temperature must be reached experimentally to form a BEC in the laboratory.

In this subsection we use the chemical potential and the Bose-Einstein distribution to understand how the ground state occupation N_0 responds to T. Let us start by approximating the sum over all states equation (1.6) as an integral. Note that this is only valid for the excited Bosons, as the integral does not account for the macroscopic occupation of a single state. What we are actually computing then is the occupation of the excited states $N_{exc} = N - N_0$

$$N_{exc} = \sum_{n=1} \frac{1}{e^{\beta(\epsilon_n - \mu)} - 1}. \tag{1.12}$$

In order to change the sum to an integral we consider the number of available states to be the volume of a $1/8^{th}$ sphere in n-space $\sum_n \to \frac{1}{8}\int_0^\infty 4\pi n^2 dn$ so from equation (1.9)

$$\sum_n \to \frac{\pi}{4\epsilon_1^{3/2}} \int_0^\infty \sqrt{\epsilon} d\epsilon. \tag{1.13}$$

The resulting integral however, after the continuation from a sum to an integral, is still unsolvable in general. However, if we choose the value $\mu = 0$ for the chemical potential, and also make the change of variable $x = \beta\epsilon$ we can solve in terms of the Riemann-Zeta function as

$$\begin{aligned} N_{exc} &= \frac{\pi}{4}\left(\frac{k_B T}{\epsilon_1}\right)^{3/2} \int_0^\infty \frac{\sqrt{x}}{e^x - 1} dx \\ &= \zeta(3/2)\left(\frac{\pi k_B T}{4\epsilon_1}\right)^{3/2}. \end{aligned} \tag{1.14}$$

Above the critical temperature T_C all particles are assumed to be in excited states. Assuming then that $N_{exc} = N$ along with the previous $\mu = 0$ condition we obtain

$$N = \zeta(3/2)\left(\frac{k_B T_C m}{2\hbar^2\pi}\right)^{3/2} V \tag{1.15}$$

$$\Rightarrow T_C \approx 3.31\frac{\hbar^2}{k_B m}\left(\frac{N}{V}\right)^{2/3}. \tag{1.16}$$

In the original 1995 experiment by the group of Cornell and Wieman at Boulder University [2] a condensate was formed using a vapour of ^{87}Rb atoms with molecular mass 86.909181 g/mol and number density of $2.5 \times 10^{12}\text{cm}^{-3}$. Using this result, these parameters predict a critical temperature $T_C \approx 34$nK, similar at least in magnitude to the Boulder experiment where a BEC was found to form at around 170 nK.

We can also then write the relation between the number of particles in excited states and the total atom number as

$$N_{exc} = N\left(\frac{T}{T_C}\right)^{3/2}, \tag{1.17}$$

or rather

$$\frac{N_0}{N} = 1 - \left(\frac{T}{T_C}\right)^{3/2}. \tag{1.18}$$

In figure 1.1 **(a)** we plot the relative occupancy of the ground state of a system of particles as a function of the temperature of the system. Taking inspiration from this result, and the methods discussed in [1], in figure 1.1 **(b)** we rescale this same data for Bosons by a factor of $N^{-2/3}$. We find this rescaling approximates the analytic result well for temperatures $T < T_C$.

1.1.4 Mean field theory and the Gross-Pitaevskii equation

We have seen now that the distributions of statistical mechanics can be used to determine characteristics of a BEC system in bulk, such as the relative condensate proportions and critical temperature. Many other effects in condensed Bose gases however can be understood as solutions to a type of nonlinear Schrödinger equation known as the Gross-Pitaevskii equation.

In the 1960's Eugene P. Gross [3] and Lev Pitaevskii [4] used a mean field approximation to describe the interparticle interactions in a BEC as a cubic nonlinear term added to the Schrödinger equation. The motivation here is that in a dilute gas the interactions would be weak and atoms sparse and so could be modelled as contact interactions. This lead to an effective description of the ground state collective dynamics of a weakly interacting BEC at zero temperature known as the Gross-Pitaevskii equation[3].

The GPE offers a mean field description of the condensed portion of a BEC. As the condensed atoms are all occupying the ground state of the system, the single particle wavefunctions of the BEC's constituent atoms all satisfy the GPE (1.19)

$$i\hbar\frac{\partial\psi}{\partial t} = -\frac{\hbar^2}{2m}\nabla^2\psi + V_{tr}\psi + U(t)|\psi|^2\psi. \tag{1.19}$$

The full many-body wavefunction can then be shown to minimise the model Hamiltonian from which the GPE is derived (under certain restrictions which

[3]Of notably similar form to the GPE (and originating in the same time period of the mid-20^{th} century) is the Ginzburg-Landau equation, used to model superconductivity rather than Bose condensation.

will be discussed in Chapter 2) [5]

$$H = \sum_{i=1}^{N} \left(\frac{\mathbf{p}_i^2}{2m} + V_{tr}(r_i) \right) + \frac{1}{2} \sum_{i=1}^{N} \sum_{j \neq i}^{N} V(|r_i - r_j|). \tag{1.20}$$

From the GPE a whole host of phenomena beyond Bose-Einstein condensation can be explored. Just a few examples can be found in density waves in superfluids, the propogation of light in optical fibres in the form of temporal solitons and wave propogation in non-linear media in the form of spatial solitons [6–8]. The GPE has even been used to study the flow of people in large crowds to model the phenomena of *crowd turbulence*, an effect describing potentially dangerous mass stampede effects in large crowds [9].
In one-dimensional BEC systems breathing and dipole modes can be studied. In two or three dimensions it is possible to understand vortex dynamics in terms of normal modes, stability and coupling to other oscillatory modes [10, 11]. When coupled to the Poisson equation the GPE has even been implemented in modelling a suggested alternative dark matter model, comprised of ultralight Bosons in a self gravitating BEC state [12, 13] in the galactic halo and beyond.
Beyond what is possible with the standard GPE, many adaptations and extensions exist describing more complex theories. Long-range anisotropic interactions can be modelled in terms of the Dipolar Gross-Pitaevskii equation [14–16]. Studies regarding BEC soliton dynamics exist across a range of models based on modified GPE's [17, 18] allowing dissipative processes, high density BEC's, and quantum fluctuations. For thermal fluctuations at finite temperatures, the Zaremba-Nikuni-Griffin (ZNG) formalism describes the evolution of a coupled thermal cloud and condensate [19, 20].
In all of these cases it is generally impossible in all but the most simple circumstances to exactly solve these models analytically. A range of numer-

ical methods have been applied to GPE systems with contact and dipolar interactions as well as ZNG systems, some of which will be discussed in Chapter 3 [21–26]. However, many approximations are possible to treat various systems analytically with varying levels of accuracy. Amongst the most effective methods are those coming from the calculus of variations, which we will discuss in Chapter 2. These methods are near universal in studies of GPE dynamics and there are far too many appearances in the literature to list, some of particular interest include falling BEC droplets for atom lithography [27], formation of Faraday patterns in dipolar BEC's [16], and bright solitons in cigar shaped optically trapped BEC's [28]. For now, we move on to discussing the primary focus of this thesis: adiabatic processes and shortcuts to adiabaticity.

1.2 Adiabatic processes and shortcuts to adiabaticity

In this section, we introduce the concept of adiabaticity and the quantum adiabatic theorem in quantum systems. We then outline some of the commonly used techniques for reproducing this adiabatic evolution known as a *shortcut to adiabaticity* in section 1.2.1. We give some examples from the literature of where these techniques have been implemented and the advantages gained from them in 1.2.2. We then take some time to discuss the specifics of *inverse engineering* based shortcut protocols taking a number of existing studies as examples in 1.2.3.

In quantum systems a process is described as adiabatic if it obeys the quantum adiabatic theorem. This theorem was originally stated heuristically by [29] in 1928 with regards to a change in some system parameter and the

likelihood of transitions to higher energy states as:

> *"The adiabatic theorem now states that at an infinitely slow change of the system...the transition probability remains infinitely small"*

The inverse of this statement then implies that rapid changes in a system parameter are likely to induce transitions to higher energy states. Adiabatic processes have become an essential tool in the developement of many quantum technologies for the preparation and manipulation of quantum states. However, as a consequence of the quantum adiabatic theorem, procedures implementing adiabatic evolution of states are in practice hamstrung by their long durations. Moreover, besides the logistical limitations of extending processes over exceedingly long timescales, in quantum systems decoherence can make traditional adiabatic evolution infeasible. Over the timescales associated with adiabatic passage, the desirable characteristics of a state would be lost to decoherence before the transition could be completed. This has motivated the search for faster reproduction of adiabatic evolution. Methods such as optimal control theory use numerical methods to approximate this adiabatic passage. Such methods can often achieve extremely short evolution times with low fidelity between the final and target state, however with the caveat that not all protocols may be experimentally realizable. Alternatively, some methods aim to reproduce the final state exactly using analytic methods. These analytic methods are referred to as shortcuts to adiabaticity and will be the primary focus of this thesis.

1.2.1 Methods of determining shortcut protocols

The most widely used methods of developing shortcut protocols are counterdiabatic driving [30], fast forward scaling [31], and inverse engineering [32–34]. The counterdiabatic driving method (also known as transitionless quantum driving) is based on designing time-dependent interactions, in the form of an auxiliary Hamilitonian, to force the system along an approximately adiabatic trajectory. Inverse engineering approaches instead start by designing the path of some feature of the wavefunction dynamics, then using this target path to determine the necessary path of the control parameter. Finally, fast forward methods [31] attempt to introduce a *magnification factor* to rescale the time parameter. The process then uses this infinitely large magnification factor to cancel the divergence caused by the infinitesimally slow adiabatic evolution. As a result of this cancellation it is then possible to construct a *fast forward potential* that accelerates the adiabatic evolution of the system to much shorter times.

Counterdiabatic driving and inverse engineering methods were shown to be potentially equivalent using a time dependent harmonic oscillator as an example in [35], similarly fast forward methods were compared to the inverse engineering approach in [31]. In both cases it was argued that it may be possible to interpret either method in terms of the other. The differing results then lie in the freedom of choice regarding: Invariant ansätze in the inverse engineering approach, or reference Hamiltonians in the counterdiabatic driving approach. The implication here then is that any shortcut protocol found using any of the above methods is not unique but rather a member of a family of solutions that show an overlap in their spaces of possible solutions.

1.2.2 Applications of adiabatic evolution and shortcuts to adiabaticity

Theoretical research in the area of shortcuts to adiabaticity has occurred in the context of many quantum systems, including but not limited to atom cooling methods in trapped BEC's [30, 34, 36–39], expansion and compression of trapped fermi gases [40, 41], manipulation of atoms in interacting multiparticle systems in the form of state transitions [42], contunneling and splitting in multi-well potentials [43–45] and population inversion in multi-level atomic systems [43, 46].

These methods might also find purpose in adiabatic quantum computing. References [47, 48] show implementations of Grover's search algorithm for database searches and equivalent problems as well as (3SAT) satisfiability problems based on the adiabatic evolution of a quantum mechanical system. The 3SAT problem considers a Boolean formula of a given number of clauses say $\phi = C_1 \wedge C_2 \wedge ... \wedge C_M$ where the C_i terms are clauses in conjunctive normal form in variables $x_1, ..., x_n$. It then asks whether the variables of each clause can be chosen such that the full formula ϕ evaluates to true. Reference [47] demonstrates the quadratic speedup obtained by Grovers search algorithm can be replicated using an implementation of adiabatic quantum computing. Similarly, [48] finds success in certain special cases, determining an algorithm for solving the satisfiability problem which runs in polynomial time.

More recent studies have performed calculations (similar to those relating to atom cooling) for ramps in a systems interaction strength for use in quantum heat engines. References [49] and [50] discuss the concept of a Feshbach engine driven by adiabatically varying the internal interaction strength of a system. In each of these studies the authors follow a similar procedure

as we will present in Chapter 4; taking an appropriate ansatz to fit their chosen regime, and approximating a shortcut to adiabaticity using an inverse engineering approach. Reference [50] investigates the regime of strong attractive interactions using a bright soliton type ansatz whilst [49] instead chooses a Thomas-Fermi ansatz to study strong repulsive interactions. The latter case in particular is relevant to the present work as we also make use of the Thomas-Fermi ansatz at times and reach some of the same conclusions as presented here. In our analysis, we reach the same shortcut protocol as found in [49] using a slightly different method. We discuss the efficiency with which this protocol can be implemented as well as studying the nature of any excitations which are added to the system.

1.2.3 Inverse engineering based shortcuts to adiabaticity

In Chapter 4, we will use the method of inverse engineering to derive a shortcut to adiabaticity in a BEC. In this section we provide a slightly more detailed discussion of the particulars of these methods. We also provide some examples from the literature of implementations of these methods.

As discussed previously, the inverse engineering approach consists of defining the desired boundary conditions of some feature of the wavefunction dynamics (hereafter referred to as the target parameter) over a given time span. This path is then used as a constraint in the governing equations of the system and the path of the control parameter is derived from these constraints. This method of course necessitates an analytic treatment of the governing equations.

In the context of noninteracting systems, this can be achieved by forming the

constraint or target path using invariants of the Schrödinger equation. These methods have appeared in the literature in a number of contexts ranging from the atom cooling processes discussed previously [30, 34, 36–39] to the Feshbach engine studies by [49] and [50], and accelerated forms of quantum perceptrons for quantum-enhanced machine learning [51]. A common example in the literature of these forms of inverse engineering methods are the Lewis-Reisenfeld or Ermakov-Lewis invariant based methods [52–54].

In systems described by the linear Scrödinger equation, in particular the Scrödinger equation in a harmonic trap, the analysis of the invariants of the system tends to lead to some form of *Ermakov equation* [55]

$$\ddot{b} + \omega^2(t)b = \omega_0^2/b^3 \tag{1.21}$$

, where in references [35,56] the parameter b can be shown to be proportional to the standard deviation of the wavefunction of the system ψ. In these systems it is possible to determine shortcuts to adiabaticity using the parameter b as the target parameter and the frequency ω of the trapping potential as the control parameter.

In our analysis we make use of a variational approximation to the GPE to reach an equation similar to this Ermakov equation with the addition of an order b^{-4} term

$$\ddot{b} + \omega^2(t)b = \omega_0^2/b^3 + \frac{u}{b^4}, \tag{1.22}$$

, where the u parameter determines the strength of interactions in a BEC system. This modified Ermakov equation is often referred to as the generalised Ermakov equation and has appeared in many sources including [37, 55, 57]. We then employ this inverse engineering approach to determine an approximate *quasi-adiabatic* scheme for the GPE. Rather than considering a time varying trap frequency, we instead drive the dynamics using the

interaction strength of the system as in the aforementioned Feshbach engine studies [49, 50]. From here we investigate the efficiency with which we can employ this routine with respect to the average strength of interactions in the system and the rate of decay of these efficiency curves with respect to the duration of the ramp.

1.3 Composition of thesis

This thesis will be organised as follows. Firstly, in Chapter 2 we will discuss the framework necessary for modelling such a system. We will provide a derivation of the Gross-Pitaevskii equation itself and make two variational approximations to its dynamics, one being based on the noninteracting limit and one on strong interactions. We will make a number of analytic investigations into the stationary solutions and normal modes of these variational approximations. In Chapter 3, we will discuss the numerical methods of symplectic integration and imaginary time propagation that will be necessary for numerical solutions of the Gross-Pitaevskii equation directly. We will define the quantities we will be recording over these investigations and our methods of sampling them. We will then make a similar series of calculations as those contained in Chapter 2, this time for the Gross-Pitaevskii equation as well as testing how closely our variational calculations replicate the true dynamics of the Gross-Pitaevskii equation. Finally, in Chapter 4 we will outline the derivation of our shortcut solution. We will show results of the numerical analysis in terms of a function of the energy added to the system by a given shortcut protocol. This analysis will be performed for both the variational equations and the Gross-Pitaevskii equation. We will also provide a heuristic proof for the decay exponents and frequencies of this

energy function.

Regarding the originality of the material presented in this document, in Chapters 2 and 3 we will discuss existing results and methods as background material. In Chapter 4, we derive an interaction ramp which has appeared recently in the literature in [49] using a slightly different method. The analysis of the decay and frequency of these interaction ramps as well as the exact two-dimensional ramp is, to the best of our knowledge, original material.

Chapter 2

Variational study of the Gross-Pitaevskii equation

2.1 Overview

In this chapter we will use methods of the calculus of variations to derive and study the Gross-Pitaevskii equation in terms of normal mode frequencies. These methods will be necessary background for our derivation and analysis of shortcuts to adiabaticity in Chapter 4.

First we will provide a derivation for the GPE in section 2.2, both time dependent and independent varieties. We will compute the energy functional obeyed by a wavefunction satisfying the GPE in 2.2.2. We will then take a brief aside to discuss the correspondence between ground state solutions of partial differential equations and Euler-Lagrange equations in 2.3. Following this we will apply these variational methods by using two wavefunction ansätze for the GPE to calculate equations of motion approximating GPE dynamics. We will calculate upper and lower bounds for the characteristic

frequencies of normal modes in these equations at the non-interacting ($U = 0$) and Thomas-Fermi ($U >> 1$) limits in section 2.4. We will then use numerical ODE methods to solve these systems of ODE's for the component widths of a BEC in the variational regime in section 2.5. We will give examples of breathing and quadrupole normal modes in 2.5.1 and 2.5.2 respectively and show the variance in the frequencies of these normal modes with varying interaction strengths. In 2.5.3 we will also briefly discuss some some resonant like behaviour which occurs when the interaction strength of the system is modulated [16, 58].

2.2 Derivation of the Gross-Pitaevskii equation

In deriving the Gross-Pitaevskii equation, two important assumptions regarding the behaviour of a BEC must be made. Firstly, we assume the system is at zero temperature. Secondly, the system is assumed to be dilute, with the distance between particles remaining much larger than the scattering length of particles. Together, these assumptions allow us to make a mean field approximation to the many body wavefunction.

2.2.1 Minimising the Landau potential

Here we provide a derivation of the GPE via minimisation of the Landau potential [5]. We begin by considering the model Hamiltonian for a dilute gas of trapped Bosons

$$\hat{H} = \sum_{i=1}^{N} \left(\frac{\mathbf{p}_i^2}{2m} + V_{tr}(\mathbf{x}) \right) + \frac{1}{2} \sum_{\substack{i,j=1 \\ i \neq j}} V(|\mathbf{x}_i - \mathbf{x}_j|). \tag{2.1}$$

Here we define the spatial region the wavefunction ψ exists in as $\Omega \subset \mathbb{R}^D$, some subset $\mathbf{x} \in \Omega$, $V_{tr}(\mathbf{x})$ as the trapping potential and $V(|\mathbf{x}_i - \mathbf{x}_j|)$ as the interaction potential corresponding to a contact interaction between two particles. We minimise the energy of said Hamiltonian via the thermodynamic Landau or Grand potential ϕ_G defined as

$$\begin{aligned} \phi_G &\stackrel{\text{def}}{=} U - TS - \mu N \\ &= \langle \hat{H} \rangle_\Psi - \mu \langle \Psi | \Psi \rangle, \quad T = 0. \end{aligned} \tag{2.2}$$

The many body wavefunction of the system as a whole is composed of single particle wavefunctions $\psi_i(\mathbf{x}_i)$ as $|\Psi(\mathbf{x}_1, ..., \mathbf{x}_N)\rangle = |\psi_1(\mathbf{x}_1)\rangle \otimes ... \otimes |\psi_N(\mathbf{x}_N)\rangle$. Since we have assumed $T = 0$ the single particle states ψ_i are all the ground state and so we can drop the labels to give us the mean field interpretation of the many body wavefunction

$$|\Psi\rangle = |\psi\rangle \otimes |\psi\rangle \otimes ... \otimes |\psi\rangle .$$

Calculating each term in the Landau potential one at a time we have

$$\begin{aligned} \left\langle \sum_{i=1}^{N} \frac{\mathbf{p}_i^2}{2m} \right\rangle_\Psi &= \sum_{i=1}^{N} \frac{\hbar^2}{2m} \int_\Omega \nabla\psi^*(\mathbf{x}_i) \nabla\psi(\mathbf{x}_i) d\mathbf{x}_i \\ &= N \frac{\hbar^2}{2m} \int_\Omega |\nabla\psi(\mathbf{x})|^2 d\mathbf{x} \\ &= -N \frac{\hbar^2}{2m} \int_\Omega \psi^*(\mathbf{x}) \nabla^2 \psi(\mathbf{x}) d\mathbf{x} \end{aligned} \tag{2.3}$$

, where we have integrated by parts in the final line. The potential term is then simply

$$\left\langle \sum_{i=1}^{N} V_{tr}(\mathbf{x}_i) \right\rangle_\Psi = N \int \psi^*(\mathbf{x}) V_{tr}(\mathbf{x}) \psi(\mathbf{x}) d\mathbf{x}. \tag{2.4}$$

The interaction term comes to

$$\begin{aligned}\left\langle \frac{1}{2}\sum_{\substack{i,j=1\\ i\neq j}} V(|\mathbf{x}_i-\mathbf{x}_j|)\right\rangle_{\Psi} \\ &= \frac{1}{2}\sum_{\substack{i,j=1\\ i\neq j}}\int_\Omega d\mathbf{x}_i\int_\Omega d\mathbf{x}_j\psi^*(\mathbf{x}_i)\psi^*(\mathbf{x}_j)V(|\mathbf{x}_i-\mathbf{x}_j|)\psi(\mathbf{x}_i)\psi(\mathbf{x}_j) \\ &= \frac{N(N-1)}{2}\int_\Omega d\mathbf{x}\int_\Omega d\mathbf{x}'\psi^*(\mathbf{x})\psi^*(\mathbf{x}')V(|\mathbf{x}-\mathbf{x}'|)\psi(\mathbf{x})\psi(\mathbf{x}'). \end{aligned} \tag{2.5}$$

The chemical potential term is

$$\mu\langle\Psi|\Psi\rangle = \mu\left(\int_\Omega \psi^*(\mathbf{x})\psi(\mathbf{x})d\mathbf{x}\right)^N. \tag{2.6}$$

Now considering ψ and ψ^* as independent fields we calculate a variation in ϕ_G by taking functional derivatives of equations (2.3)-(2.6). Firstly, the kinetic term

$$\frac{\delta}{\delta\psi^*}\left(-N\frac{\hbar^2}{2m}\int_\Omega \psi^*(\mathbf{x})\nabla^2\psi(\mathbf{x})d\mathbf{x}\right) = N\int_\Omega -\frac{\hbar^2}{2m}\nabla^2\psi(\mathbf{x})\delta\psi^*(\mathbf{x})d\mathbf{x}. \tag{2.7}$$

The variation of the trapping potential term is

$$\frac{\delta}{\delta\psi^*}\left(N\int_\Omega \psi^*(\mathbf{x})V_{tr}(\mathbf{x})\psi(\mathbf{x})d\mathbf{x}\right) = N\int_\Omega V_{tr}(\mathbf{x})\psi(\mathbf{x})\delta\psi^*(\mathbf{x})d\mathbf{x}. \tag{2.8}$$

The variation of the contact interactions term is

$$\begin{aligned}&\frac{\delta}{\delta\psi^*}\left(\frac{N(N-1)}{2}\int_\Omega d\mathbf{x}\int_\Omega d\mathbf{x}'\psi^*(\mathbf{x})\psi^*(\mathbf{x}')V(|\mathbf{x}-\mathbf{x}'|)\psi(\mathbf{x})\psi(\mathbf{x}')\right) \\ &= N(N-1)\int\delta\psi^*(\mathbf{x})\left(\int|\psi(\mathbf{x})|^2V(|\mathbf{x}-\mathbf{x}'|)d\mathbf{x}'\right)\psi(\mathbf{x})d\mathbf{x}. \end{aligned} \tag{2.9}$$

Then finally the variation of the chemical potential term is

$$\begin{aligned}\frac{\delta}{\delta\psi^*}\left(\mu\int_\Omega \psi^*(\mathbf{x})\psi(\mathbf{x})d\mathbf{x}\right)^N &= \mu N\left(\int_\Omega \psi^*(\mathbf{x})\psi(\mathbf{x})d\mathbf{x}\right)^{N-1}\left(\int_\Omega \delta\psi^*(\mathbf{x})\psi(\mathbf{x})d\mathbf{x}\right) \\ &= \mu N\int_\Omega \delta\psi^*(\mathbf{x})\psi(\mathbf{x})d\mathbf{x} \end{aligned} \tag{2.10}$$

, as the single particle wavefunctions are normalised to one. In addition, note the dummy variables x and x' are relabelled after the differentiation step in each of (2.7)-(2.10). When we put all the terms together we find the variation of the Landau potential is given by

$$\frac{\delta\phi_G}{\delta\psi^*} = N\int_\Omega \Bigg\{ -\frac{\hbar^2}{2m}\nabla^2\psi(\mathbf{x}) + V_{tr}(\mathbf{x})\psi(\mathbf{x}) \\ +(N-1)\left(\int_\Omega |\psi(\mathbf{x})|^2 V(|\mathbf{x}-\mathbf{x}'|)d\mathbf{x}'\right)\psi(\mathbf{x}) - \mu\psi(\mathbf{x})\Bigg\}\delta\psi^*(\mathbf{x})d\mathbf{x} = 0. \quad (2.11)$$

If the variation is to vanish then by the fundamental lemma of the calculus of variations the terms in braces must also be zero, leading to the time independent GPE (2.12). Since N is usually large it is common to make the approximation $N \approx N-1$. As $V(|x-x'|)$ is modelling contact interactions we assume it has a delta function form ie. $V(|x-x'|) = \frac{4\pi\hbar^2}{m}a\delta(x-x')$ with a being the s-wave scattering length. It is then convenient to absorb these constants into the parameter U encapsulating the strength of contact interactions in the system giving us

$$-\frac{\hbar^2}{2m}\nabla^2\psi(\mathbf{x}) + V_{tr}(\mathbf{x})\psi(\mathbf{x}) + U|\psi(\mathbf{x})|^2\psi(\mathbf{x}) = \mu\psi(\mathbf{x}). \quad (2.12)$$

Applying the unitary time evolution operator we find the time dependent version in $\psi(x,t)$

$$i\hbar\frac{\partial\psi(\mathbf{x},t)}{\partial t} = -\frac{\hbar^2}{2m}\nabla^2\psi(\mathbf{x},t) + V_{tr}(\mathbf{x})\psi(\mathbf{x},t) + U|\psi(\mathbf{x},t)|^2\psi(\mathbf{x},t). \quad (2.13)$$

2.2.2 Energy density

The energy of the wavefunction described by (2.12) and (2.13) is given by equations (2.3)-(2.5). For clarity, when we combine these equations we have

the total energy functional

$$E[\psi] = \int_\Omega \left(-\frac{\hbar^2}{2m}\psi^*(\mathbf{x},t)\nabla^2\psi(\mathbf{x},t) + \psi^* V_{tr}(\mathbf{x},t)\psi(\mathbf{x},t) \right) d\mathbf{x} + \int_\Omega d\mathbf{x} \int_\Omega d\mathbf{x}' \frac{N-1}{2} V(|x-x'|)|\psi(\mathbf{x},t)|^2 |\psi(\mathbf{x}',t)|^2. \tag{2.14}$$

After inserting the form of $V(|\mathbf{x}-\mathbf{x}'|)$ used in equation (2.12) and integrating over the delta function this leads to the total energy

$$E[\psi] = \int_\Omega \left(\frac{\hbar^2}{2m}|\nabla\psi(\mathbf{x},t)|^2 + V_{tr}(\mathbf{x})|\psi(\mathbf{x},t)|^2 + \frac{U}{2}|\psi(\mathbf{x},t)|^4 \right) d\mathbf{x}. \tag{2.15}$$

The energy density, ie. the integrand of the above, is not a conserved quantity, the total energy itself however is conserved under time evolution which we can see by differentiating with respect to time

$$\frac{dE}{dt} = \int_\Omega \dot{\psi}(\mathbf{x},t) \left(-\nabla^2\psi(\mathbf{x},t)^* + V_t r(\mathbf{x})\psi(\mathbf{x},t)^* + \frac{U}{2}|\psi(\mathbf{x},t)|^2\psi(\mathbf{x},t)^* \right) d\mathbf{x} + \text{h.c.}. \tag{2.16}$$

The GPE gives us $\dot{\psi}$ and $\dot{\psi}^*$ so we find

$$\frac{dE}{dt} = \int_\Omega -i \left| \left(-\frac{\hbar}{2m}\nabla^2\psi(\mathbf{x},t) + V_{tr}(\mathbf{x})\psi(\mathbf{x},t) + \frac{U}{2}|\psi(\mathbf{x},t)|^2\psi(\mathbf{x},t) \right) \right|^2 + i \left| \left(-\frac{\hbar}{2m}\nabla^2\psi(\mathbf{x},t) + V_{tr}(\mathbf{x})\psi(\mathbf{x},t) + \frac{U}{2}|\psi(\mathbf{x},t)|^2\psi(\mathbf{x},t) \right) \right|^2 = 0. \tag{2.17}$$

2.3 Variational calculations

The variational method of solving certain partial differential equations involves recognising the solution of a given PDE as the extremum of an associated energy functional. This minimiser can then be found by computing the Euler-Lagrange equations of the system given a suitable ansatz. The proof of existence and uniqueness of minimisers requires more careful functional

analysis and is beyond the scope of this thesis. However, a detailed discussion of these problems with respect to the Gross-Pitaevskii can be found in [59] and [60] respectively where it is shown that so long as the trapping potential satisfies some criteria at the boundaries as $x \to \infty$ and $U \in [0, U^*)$ for some cut-off value U^* there exists a unique minimiser of equation (2.12). Here we assume some function u is a minimiser of a general functional L and show that this function also satisfies the Euler-Lagrange equations (1) [61, 62].

Theorem 1. *For some interval in time $\tau \subset \mathbb{R}$ and a given functional $L(\omega', \omega, \tau)$ where the $'$ represents differentiation with respect to τ, consider some action $I_L(\omega)$*

$$I_L(\omega) = \int_\tau L(\omega', \omega, t)dt. \tag{2.18}$$

Let $\mathcal{A} = \{\omega(\tau) \in C^2, \omega(t) = 0 : t \in \partial\tau\}$ be the family of functions which are continuous and twice differentiable on the interval τ. Let $u \in \mathcal{A}$ be a minimiser of the action $I_L(\omega)$. This function u is then also a solution to the corresponding Euler-Lagrange equations

$$\frac{\partial L}{\partial u}(u', u, t) - \frac{d}{dt}\frac{\partial L}{\partial u'}(u', u, t) = 0. \tag{2.19}$$

Consequently, u then also solves the partial differential equation to which the functional $L(\omega)$ corresponds.

Proof. Consider a perturbation of the function $u(t)$ for a small parameter ϵ and some function $v(t) \in \mathcal{A}$ defined as $i(\epsilon) = u(t) + \epsilon v(t)$. The perturbed action is then

$$I_L(i(\epsilon)) = \int_\tau L(t, i(\epsilon), i'(\epsilon))dt = \int_\tau L_\epsilon dt. \tag{2.20}$$

If u is a minimiser of I_L then $I_L'(i(0)) = 0$ so

$$\frac{dI_L}{d\epsilon} = \int_\tau \frac{dL_\epsilon}{d\epsilon}dt \tag{2.21}$$

$$= \int_\tau v(t)\frac{\partial L_\epsilon}{\partial i(\epsilon)} + v'(t)\frac{\partial L_\epsilon}{\partial i'(\epsilon)}dt. \tag{2.22}$$

Which when evaluated at $\epsilon = 0$ is

$$I'_L(i(0)) = \int_\Omega v(t)\frac{\partial L}{\partial u} + v'(t)\frac{\partial L}{\partial u'}dt = 0. \tag{2.23}$$

Integrating by parts over the second term this becomes

$$\int_\tau v(t)\frac{\partial L}{\partial u}dt + \left[v(t)\cdot\frac{\partial L}{\partial u'}\right]_{t=\partial\tau} - \int_\tau v(t)\frac{d}{dt}\frac{\partial L}{\partial u'}dt = 0. \tag{2.24}$$

The boundary term is zero owing to the compactness condition on v so

$$\int_\Omega v(t)\left(\frac{\partial L}{\partial u} - \frac{d}{dt}\frac{\partial L}{\partial u'}\right)dt = 0. \tag{2.25}$$

Since this is true for all $v \in \mathcal{A}$ we conclude via the fundamental lemma of calculus of variations that the function u solves the Euler-Lagrange equations

$$\frac{\partial L}{\partial u}(u', u, t) - \frac{d}{dt}\frac{\partial L}{\partial u'}(u', u, t) = 0. \tag{2.26}$$

□

In the following two sections, we choose two different ansätze, one valid at small values of U, and one valid at large U. We then exploit the correspondence discussed here to derive equations of motion for the parameters of our chosen ansatz. The relevant functional is the Lagrangian density of a complex scalar field with a harmonic potential and contact interactions. The corresponding action is the spatial integral of said Lagrangian density

$$\begin{aligned}\mathcal{L}(\nabla\psi, \frac{\partial\psi}{\partial t}, \psi, \mathbf{x}) =& \frac{i}{2}\left(\psi^*(\mathbf{x}, t)\frac{\partial\psi(\mathbf{x})}{\partial t} - \psi(\mathbf{x})\frac{\partial\psi^*(\mathbf{x})}{\partial t}\right) \\ &- \frac{1}{2}|\nabla\psi(\mathbf{x})|^2 - V_{tr}(\mathbf{x})|\psi(\mathbf{x})|^2 - \frac{U}{2}|\psi(\mathbf{x})|^4.\end{aligned} \tag{2.27}$$

2.3.1 Gaussian ansatz

The non-interacting Schrödinger equation is solved by a Gaussian ansatz, at small U this should approximate the ground state of the GPE. The first

ansatz we choose is a Gaussian of widths σ_i in each dimension of the space x_i and respective phases β_i

$$\psi(\mathbf{x}, \sigma_i, \dot{\sigma}_i, \beta_i, \dot{\beta}_i) = \mathcal{N}(\sigma, \beta) \exp\left(\sum_i -\frac{x_i^2}{2\sigma_i^2} - i\beta_i x_i^2\right) \tag{2.28}$$

, where $\mathbf{x}$ is the spatial vector $\mathbf{x} = (x_1, ..., x_D)$ for dimension D. The normalisation factor $\mathcal{N}$ comes to $\mathcal{N} = \Pi_{i=1}^{D}(\sigma_i \pi^{1/2})^{-1/2}$. Note the results of this section hold for dimension $D \in \{1, 2, 3\}$. As a reminder, the Lagrangian we want to minimise is

$$\begin{aligned} L = \frac{i}{2}\int_\Omega \psi^*(\mathbf{x}, t)\partial_t\psi(\mathbf{x}, t) - \psi(\mathbf{x}, t)\partial_t\psi^*(\mathbf{x}, t) \\ - \frac{1}{2}|\nabla\psi(\mathbf{x}, t)|^2 - V_{tr}(\mathbf{x})|\psi(\mathbf{x}, t)|^2 - \frac{U}{2}|\psi(\mathbf{x}, t)|^4 d\mathbf{x}. \end{aligned} \tag{2.29}$$

We have introduced the harmonic trapping potential $V_{tr}(\mathbf{x})$ defined as

$$V_{tr}(\mathbf{x}) = \frac{1}{2}\left(\Omega_1^2 x^2 + \Omega_2^2 y^2 + \Omega_3^2 z^2\right) \tag{2.30}$$

, for a three dimensional system. Note that the trapping frequencies Ω_i have no relation to the function space Ω. After calculating this Lagrangian using the anisotropic ansatz equation (2.28) we find

$$L_G = \sum_{i=1}^{D}\left(\frac{\dot{\beta}_i\sigma_i^2}{2} - \frac{1}{4\sigma_i^2} - \beta_i^2\sigma_i^2 - \frac{\Omega_i^2\sigma_i^2}{4}\right) - \frac{U}{2}\frac{1}{(2\pi)^{D/2}}\prod_{i=1}^{D}\sigma_i^{-1}. \tag{2.31}$$

This leads to a system of $2 \times D$ ODE's in σ_i and β_i

$$\dot{\sigma}_i = -2\beta_i\sigma_i, \tag{2.32}$$

$$\dot{\beta}_i\sigma_i + \frac{1}{2\sigma_i^3} - 2\beta_i^2\sigma_i - \frac{\Omega_i^2\sigma_i}{2} + \frac{U}{2}\frac{1}{(2\pi)^{D/2}}\frac{1}{\sigma_i}\prod_{j=1}^{D}\sigma_j^{-1} = 0. \tag{2.33}$$

Solving the first D equations for the phase parameters β_i and then computing $\dot{\beta}_i$ gives

$$\beta_i = -\frac{\dot{\sigma}_i}{2\sigma_i} \quad \dot{\beta}_i = \frac{\dot{\sigma_i^2}}{2\sigma_i^2} - \frac{\ddot{\sigma}_i}{2\sigma_i}. \tag{2.34}$$

Using these expressions we eliminate the phase dependence from the second D equations giving us the system of equations for σ_i where $i = (1, ..., D)$,

$$\sigma_i \ddot{\sigma}_i + \Omega_i^2 \sigma_i^2 - \frac{1}{\sigma_i^2} = \frac{U}{(2\pi)^{D/2}} \prod_{j=1}^{D} \sigma_j^{-1}. \tag{2.35}$$

With energy given by

$$E = \frac{1}{4} \sum_{i=1}^{D} \left(\dot{\sigma}_i^2 + \frac{1}{\sigma_i^2} + \Omega_i^2 \sigma_i^2 \right) + \frac{U}{2(2\pi)^{D/2}} \prod_{j=1}^{D} \sigma_j^{-1}. \tag{2.36}$$

Isotropic motion

In the case where only breathing mode type oscillations are present and the trapping potential is isotropic, ie. $\Omega_1 = \Omega_2 = \Omega_3 = \Omega$, we may impose $\sigma_1 = \sigma_2 = \sigma_3 = \sigma$. The system of equations (2.35) reduces to a single equation,

$$\sigma \ddot{\sigma} + \Omega^2 \sigma^2 - \frac{1}{\sigma^2} = \frac{U}{(2\pi)^{D/2}} \frac{1}{\sigma^D}. \tag{2.37}$$

Similarly, the energy of the system (2.36) reduces to,

$$E = \frac{D}{4} \left(\dot{\sigma}^2 + \frac{1}{\sigma^2} + \Omega^2 \sigma^2 \right) + \frac{U}{2(\sqrt{2\pi}\sigma)^D}. \tag{2.38}$$

The system described by this isotropic equation of motion would describe a breathing mode in the GPE, with each component $(\sigma_1, \sigma_2, \sigma_3)$ oscillating in phase with the other.

2.3.2 Thomas-Fermi ansatz

The Thomas-Fermi approximation is applicable to BEC's with either very large total atom number N or very strong interactions U. In either of these cases, the kinetic energy term in the GPE may be neglected, leading to a simple solution for the wavefunction $\psi(\mathbf{x})$. To see this, we begin with the

time independent GPE (2.12):

$$\mu\psi(\mathbf{x}) = -\frac{\hbar^2}{2m}\nabla^2\psi(\mathbf{x}) + V_{tr}(\mathbf{x})\psi(\mathbf{x}) + U|\psi(\mathbf{x})|^2\psi(\mathbf{x}). \tag{2.39}$$

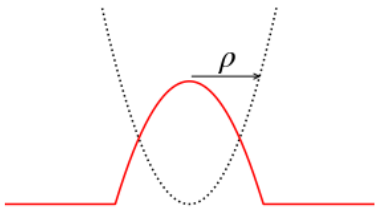

Figure 2.1: Width of wavefunction in a harmonic trap.

By introducing some parameter ρ as a heuristic measure of the size of the condensate cloud we can estimate the average energy contributions from the kinetic, potential, and interaction terms in one dimensional systems,

$$E_K \sim \frac{\hbar^2}{2m\rho^2}, \tag{2.40}$$

$$E_P \sim \frac{m\omega^2\rho^2}{2}, \tag{2.41}$$

$$E_I \sim \frac{UN}{\rho}. \tag{2.42}$$

Both the kinetic and interaction terms increase the energy of the cloud as the radius decreases, meaning that each of these terms tend to force the cloud to expand. Since both of these terms act in the same direction, if one is much greater than the other then neglecting one accumulates relatively little error. The Thomas-Fermi approximation is valid if and only if the condition $E_I >> E_K$ is met. In terms of (2.40)-(2.42) this condition becomes

$$\frac{UN}{\rho} >> \frac{\hbar^2}{2m\rho^2}. \tag{2.43}$$

The cloud size ρ is a monotonically increasing function of U for repulsive interactions as the interactions act to expand the cloud. This behaviour of $\rho(U)$ along with imposing the normalisation condition $N = ||\psi|| = 1$ and adopting units $\hbar = m = 1$ means the condition which must be satisfied is

$$U >> 1. \tag{2.44}$$

Assuming we are in this large U regime, we can write an asymptotic solution to (2.12) as

$$\psi(\mathbf{x}) = \left(\frac{3}{4}\frac{\rho^2 - x^2}{\rho^3}\right)^{1/2}. \tag{2.45}$$

Using this as our ansatz, we compute from the complex scalar field Lagrangian, the Thomas-Fermi Lagrangian (2.46) (this time in just one dimension),

$$L_{TF} = \frac{\rho^2\dot{\beta}}{5} - \frac{2\rho^2\beta^2}{5} - \frac{\Omega^2\rho^2}{10} - \frac{3U}{10\rho}. \tag{2.46}$$

Which by theorem (1) has minimisers ρ and β satisfying the system of equations

$$\beta = -\frac{\dot{\rho}}{2\rho}, \tag{2.47}$$

$$\rho\dot{\beta} - 2\rho\beta^2 - \frac{\Omega^2\rho}{2} + \frac{3U}{4\rho^2} = 0. \tag{2.48}$$

Computing the phase parameter derivative $\dot{\beta}$ from the first equation, we can rewrite this as a single second order differential equation in ρ,

$$\rho\ddot{\rho} + \Omega^2\rho^2 = \frac{3U}{2\rho}. \tag{2.49}$$

We can also compute the energy of a state following (2.49) as

$$E(\rho) = \frac{\dot{\rho^2}}{10} + \frac{\Omega^2\rho^2}{10} + \frac{3U}{10\rho}. \tag{2.50}$$

2.4 Normal modes of the variational equations

Now that we have reduced the GPE to a significantly simpler set of ordinary differential equations, we would like to understand the normal modes we expect the system to exhibit under time evolution. We soon solve the

equations numerically for this purpose, but some analytic methods may also be employed as limiting cases in the $U = 0$ non interacting and $U >> 1$ Thomas-Fermi regimes of the variational equations.
Since the Thomas-Fermi variational equation (2.49) is a limiting case for the Gaussian variational equation (2.35) there will be no variation in the charactistic frequencies of its normal modes. The Thomas-Fermi equation can be shown to have a constant breathing mode frequency for all U given by equation (2.52). For this reason the remainder of this section will concern normal modes of the Gaussian equations (2.35).

2.4.1 Characteristic frequency of the breathing mode via oscillatory ansatz

As we are interested in studying the breathing mode only in this section, we make the following calculations using the isotropic Gaussian variational equation (2.37). We approximate the frequency ω of the breathing mode in the Gaussian equation by linearising equation (2.37). We make the secondary ansatz $\sigma(t) = \sigma^0 + \Sigma\cos(\omega t)$ and expand in powers of Σ/σ^0. Assuming the oscillations are relatively small, and the trapping potential is isotropic, this approximation is valid. Firstly, we consider the noninteracting case. Inserting the oscillatory ansatz into equation (2.37) with $U = 0$ leads to the frequency $\omega = 2$ as

$$\begin{aligned} &\left(\omega^2\Sigma + \Sigma + 3\Sigma\right)\cos(\omega t) = 0, \\ &\Rightarrow \omega = 2, U = 0. \end{aligned} \tag{2.51}$$

We note here that this procedure applied to the Thomas Fermi equation also yields this same frequency but for all U as we expected.

We use a similar process to approximate the breathing frequency in the large U limit. As discussed relating to the Thomas-Fermi approximation to the GPE in section 2.3.2, at large values of U we can neglect the kinetic term in the GPE. The corresponding term in the Gaussian variational equation is σ^{-2}. By dropping this σ^{-2} in the Gaussian variational equation and then taking the oscillatory ansatz we find the breathing frequency at large values of U

$$\omega = \sqrt{D+2}, U >> 1. \tag{2.52}$$

We also note that when the Gaussian variational equation (2.37) is considered in two dimensions it has an exact analytic solution as well as a constant breathing frequency of $\omega = 2$ independent of U. We make use of this fact in section 4.2.5 when determining exact shortcuts to adiabaticity in a two-dimensional system. A discussion of the relation between this constant frequency breathing mode and a symmetry of the underlying $SO(2,1)$ Lorentz group is available in [63].

2.4.2 Spectrum of normal modes via the Hessian matrix

In this section we perform a more thorough analysis of the normal modes present in the anisotropic Gaussian equation (2.35).

The normal modes of a dynamic system of several variables can be studied using the Hessian matrix. The Hessian matrix is formed of the second derivatives of the potential energy function as $\Lambda_{ij} = \frac{\partial^2 U}{\partial \sigma_i \partial \sigma_j}$. Consider a dynamical system of the form $\ddot{q}_i = f(q_1, ..., q_n)$ with potential energy $V(q)$

and a stationary point at q^0 which is assumed to be zero,

$$\begin{aligned} V(q) =& V(0) + \frac{1}{2}\sum_{j,k} q_j \frac{\partial^2 U}{\partial q_j \partial q_k}\Big|_{q_j=0, q_k=0} q_k \\ =& V(0) + \frac{1}{2}\sum_{j,k} q_j \Lambda_{jk} q_k. \end{aligned} \tag{2.53}$$

We form Newtons equation $\dot{p} = -\nabla V$ by calculating the force along the j^{th} canonical coordinate as $F_j = -\nabla V = -\sum_k \Lambda_{jk} q_k$ using the expanded version of $V(q)$ given above. The momentum term along the j^{th} coordinate is $\ddot{q}_j$ so we have

$$\ddot{q}_j = -\sum_k \Lambda_{jk} q_k. \tag{2.54}$$

We then take an oscillatory ansatz $q = q^0 + Q\cos(\omega t)$, as we are concerned with the normal modes of vibration, to find the eigenvalue equation

$$\omega_j^2 x_j = \sum_k \Lambda_{jk} x_k \tag{2.55}$$

, where ω_j^2 and x_j are the eigenvalues and eigenvectors of Λ_{jk}.
By applying this principle to the Gaussian variational equations, we may compute the normal mode frequencies as the square root of the eigenvalues of Λ_{ij}.

The Gaussian equation (2.35) has total energy function

$$E = \frac{1}{4}\left(\sum_i^D \dot{\sigma_i^2} + \frac{1}{\sigma_i^2} + \Omega_i^2 \sigma_i^2\right) + \frac{U}{2(2\pi)^{D/2}} \prod_j^D \frac{1}{\sigma_j}. \tag{2.56}$$

The potential energy then follows as

$$V(\sigma_i) = \frac{1}{4}\left(\sum_i^D \frac{1}{\sigma_i^2} + \Omega_i^2 \sigma_i^2\right) + \frac{U}{2(2\pi)^{D/2}} \prod_j^D \frac{1}{\sigma_j}. \tag{2.57}$$

When calculated in the Thomas-Fermi limit, ie. after dropping the $\frac{1}{\sigma_i^2}$term, the diagonal terms of the Hessian matrix are

$$\Lambda_{ii} = \left(\Omega^2 + \frac{2u}{\sigma_i^2} \prod_n^D \frac{1}{\sigma_n}\right)\Big|_{\sigma_i = \sigma_i^0 \,,\, i=(1,\ldots,D)} \tag{2.58}$$

, where σ_i^0 is the ground state value of σ_i and u is a redefinition of U to absorb the $(2\pi)^{D/2}$ constant. The off-diagonal terms are found as

$$\Lambda_{ij} = \left(\frac{u}{\sigma_i \sigma_j} \prod_n^D \frac{1}{\sigma_n} \right) \Big|_{\sigma_i = \sigma_i^0 \, , \, i=(1,\ldots,D)} . \tag{2.59}$$

The ground state values σ_i^0 for an isotropic trap are $\sigma_i^0 = \left(\frac{u}{\Omega^2}\right)^{1/5}$ at large U meaning the full Hessian matrix is

$$\Lambda = \begin{pmatrix} 3\Omega^2 & \Omega^2 & \Omega^2 \\ \Omega^2 & 3\Omega^2 & \Omega^2 \\ \Omega^2 & \Omega^2 & 3\Omega^2 \end{pmatrix} . \tag{2.60}$$

The frequencies of associated normal modes are given by the square root of the Hessians eigenvalues. For Λ above we have eigenvalues $\lambda = 2\Omega^2; \lambda = 2\Omega^2; \lambda = 5\Omega^2$ meaning the characteristics frequencies of normal modes in three dimensions are the breathing mode $\omega_B = \sqrt{5}\Omega$ and two quadrupole modes with $\omega_Q = \sqrt{2}\Omega$.

2.5 Dynamics of the variational equations

In this section, we solve the Gaussian variational equations numerically to verify the normal mode frequencies calculated in the previous section.
We initially recreate the evolution of the wavefunction ψ by creating a mesh of normally distributed random variables in $\mathbb{R}^3$ with standard deviations σ_i given by the anisotropic equations (2.35). Some illustrative examples of these dynamical modes are given in figures 2.2 and 2.4. We perform this analysis for dynamics of the breathing mode and quadrupole mode type. We then record the characteristic frequencies of these normal modes for a range of U.

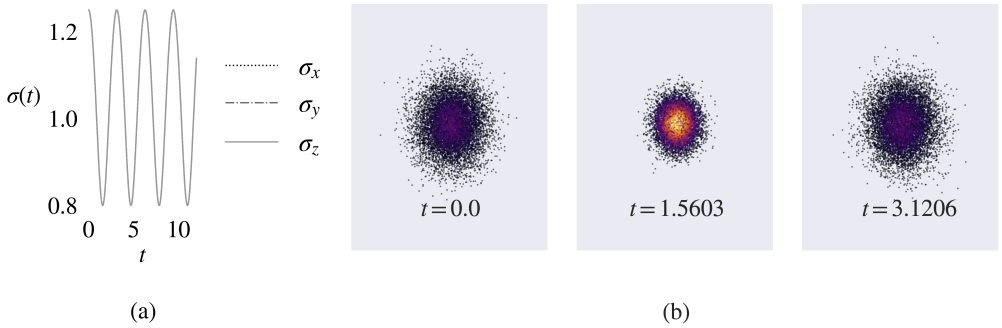

Figure 2.2: **(a)** Breathing type dynamics from Gaussian radius data using equation (2.35) for $U = 0$ and $D = 3$. **(b)** Snapshots of a sample of normally distributed random variables in $\mathbb{R}^3$ with variances shown in **(a)**.

2.5.1 Breathing mode dynamics in the Gaussian equations

We solve the anisotropic equations (2.35) for the parameters σ_i with $\sigma_x(0) = \sigma_y(0) = \sigma_z(0)$. In figure 2.2 we see the time evolution of these parameters in **(a)** and a recreation of a wavefunction density from this data in **(b)**. In figure 2.3 we show a number of sample three-dimensional systems and their Fourier decomposition as well as the relation between interaction strength and breathing mode frequencies in one, two, and three dimensions.

2.5.2 Quadrupole mode dynamics

Quadrupole dynamics occur when one of the components of σ oscillates out of phase with the others. Here we study the frequencies present when dynamics are initiated with σ_z out of phase with σ_x and σ_y. In the non-interacting system there is no coupling between each equation in (2.35) and we see

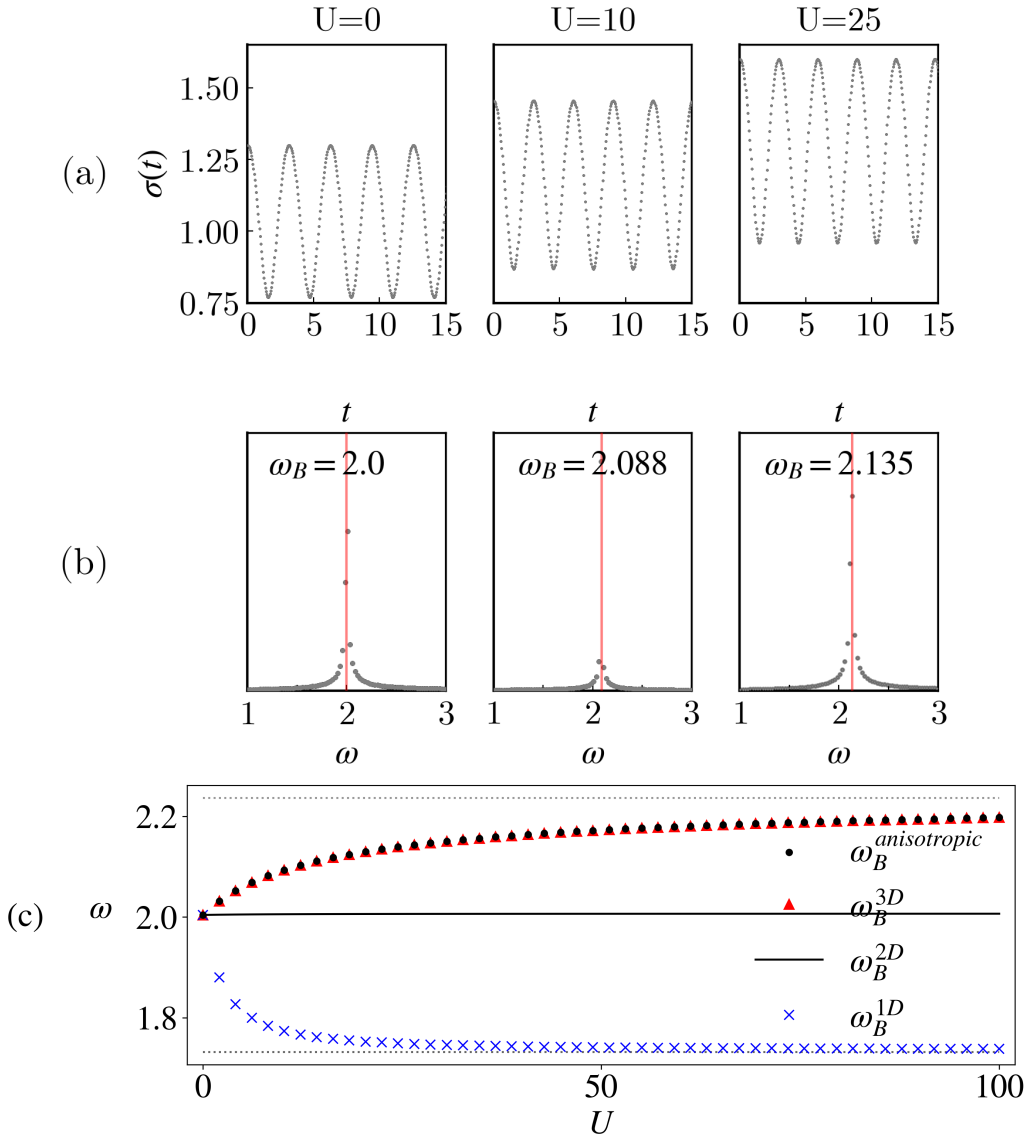

Figure 2.3: **(a)** Breathing mode ($\sigma_x = \sigma_y = \sigma_z$) radius dynamics in three dimensions. **(b)** Fourier transform frequency analysis with dominant frequency ω_B highlighted. **(c)** Breathing frequencies for $U = \{0, ..., 100\}$ using the isotropic equation of motion in $D = 1, 2, 3$ dimensions and the anisotropic equations in $D = 3$, dotted lines at $\sqrt{D+2}$.

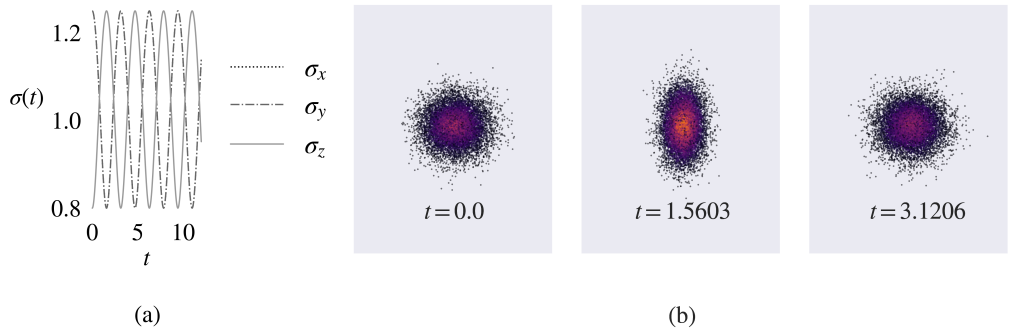

Figure 2.4: **(a)** Quadrupole type dynamics from Gaussian radius data using equation (2.35) for $U = 0$ and $D = 3$. **(b)** Snapshots of a sample of normally distributed random variables in $\mathbb{R}^3$ with variances shown in **(a)**.

regular sinusoidal oscillations independent of one another, see figure 2.4 **(a)**. As previously, we have also used a sampling of normally distributed random variables with standard deviation given by (2.35) to recreate a wavefunction undergoing quadrupole type dynamics in figure 2.4 **(b)**.
However once we consider finite interactions each component is coupled and the dynamics of one component has a distinguishable effect on the others, appearing here as a beating phenomenon. A fast Fourier transform (FFT) analysis of this data shows two distinct frequencies, one for the breathing mode and another for the quadrupole mode. Measuring these frequencies in three dimensions for a range of U we find peaks representing the breathing and quadrupole frequencies as well as a number of smaller contributions from higher harmonic frequencies shown in figure 2.5. We record the two dominant frequencies in this Fourier space data and display them versus the respective interaction strengths in figure 2.6. We can also use the beat frequency calculated from this breathing and quadrupole frequency data

to approximate an envelope above and below the radius oscillations as shown in figure 2.6

2.5.3 Resonant behaviour for time-dependent interactions

In the GPE, resonant dynamical behaviour may occur when parameters of the system are driven at frequencies close to an eigenmode of the system, ie. the breathing or quadrupole modes. The nonlinearity of the equation can then induce nonlinear responses such as harmonic generation and shifts in the frequencies of collective modes [11,16,58]. In these studies, in particular [58], the nonlinear response of a BEC described by the isotropic Gaussian equation (2.37) is studied by modulating the strength of interactions in a system and analysing the magnitude of resonant dynamics that occur. The strength of interactions is modulated as

$$U(t) = p + q\cos(\Omega t). \tag{2.61}$$

The system is initially in the ground state of the undriven $U = p$ system and, when driven with amplitude q and frequency Ω, the magnitude of the non-linear response is defined as $(\sigma_{min} - \sigma_{max})/2$. We find several responses, ranging from slight constructive and destructive interference when Ω is far from an eigenmode, to large resonant responses when the driving frequency is close to an eigenmode. In figure 2.7 we show the time dependence of σ for a number of driving frequencies. We also show the magnitude of these resonant responses versus the driving frequency Ω. We find that large amplitude resonant responses occur near the undriven normal mode frequencies ω_B and higher harmonics $2\omega_B/n, n \in \mathbb{Z}$ but offset by some amount related to the magnitude q of the driven parameter. Shifted resonant fre-

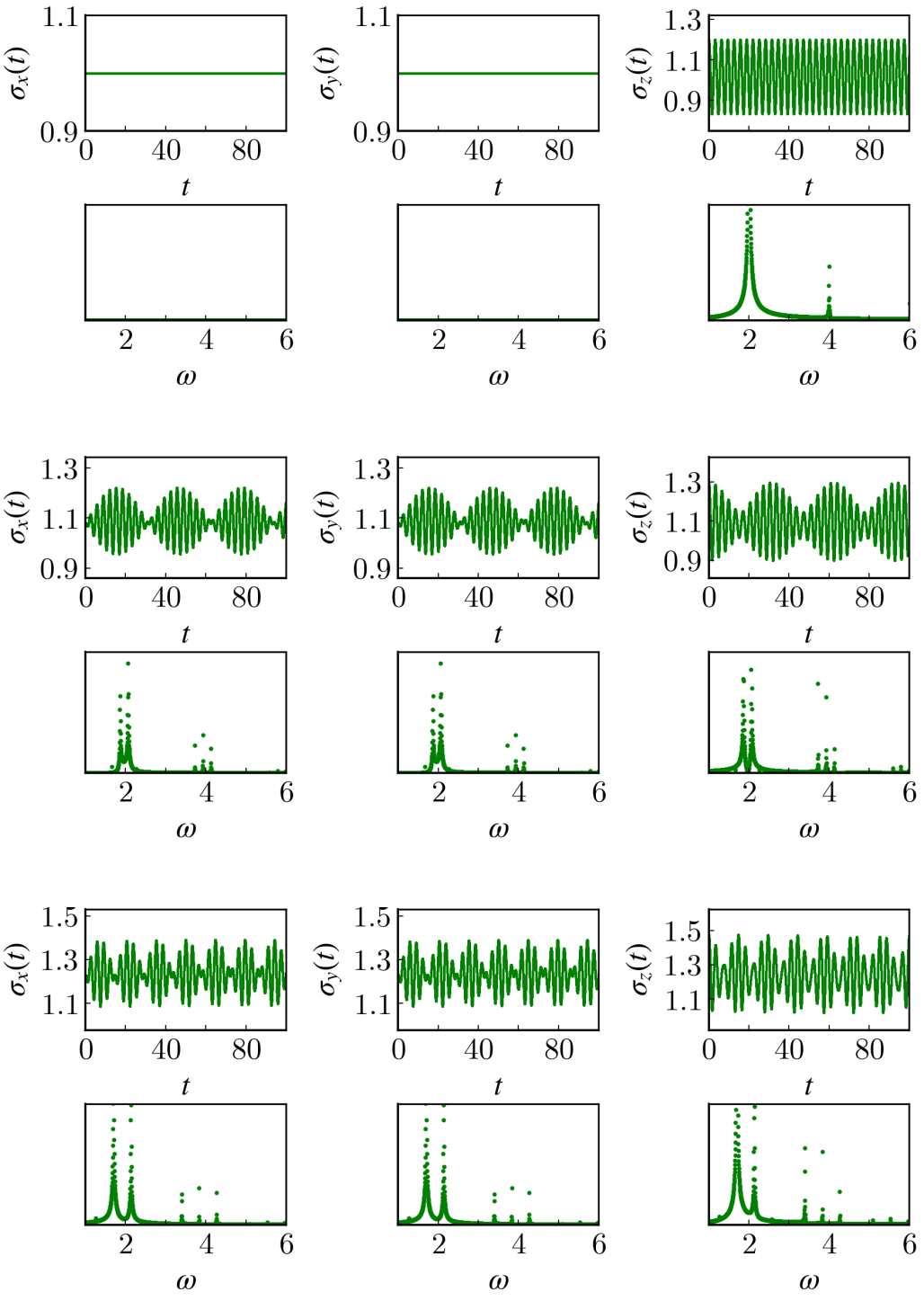

Figure 2.5: Quadrupole type dynamics and the Fourier space picture for (top two panels) $U = 0$ (centre) $U = 6$ and (lower two panels) $U = 25$, $D = 3$. Arbitrary y-axis units in Fourier space panels.

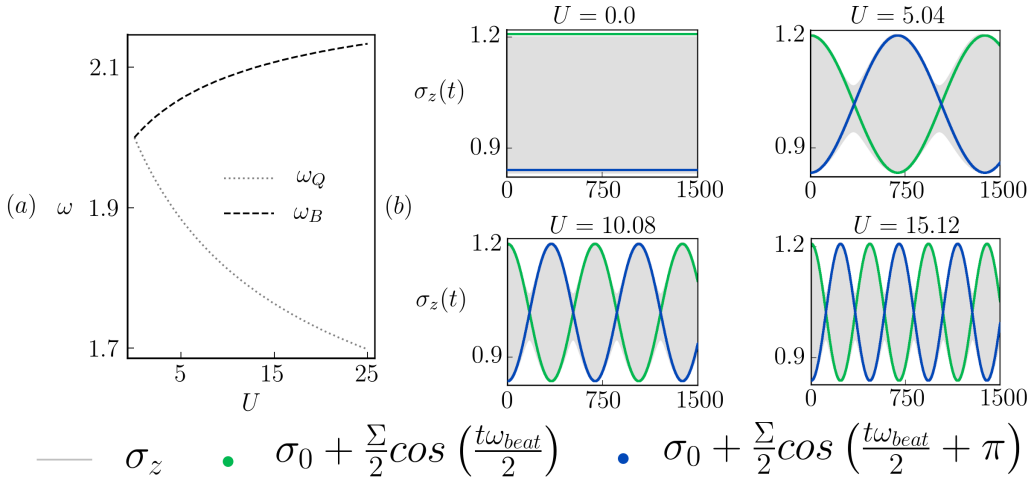

Figure 2.6: **(a)** Frequencies of the breathing and quadrupole mode for $U = \{0, ..., 25\}$. **(b)** Envelopes calculated from the difference in the breathing and quadrupole frequencies.

quencies of this form have been studied in the context of variational approximations to the GPE in [11, 58].

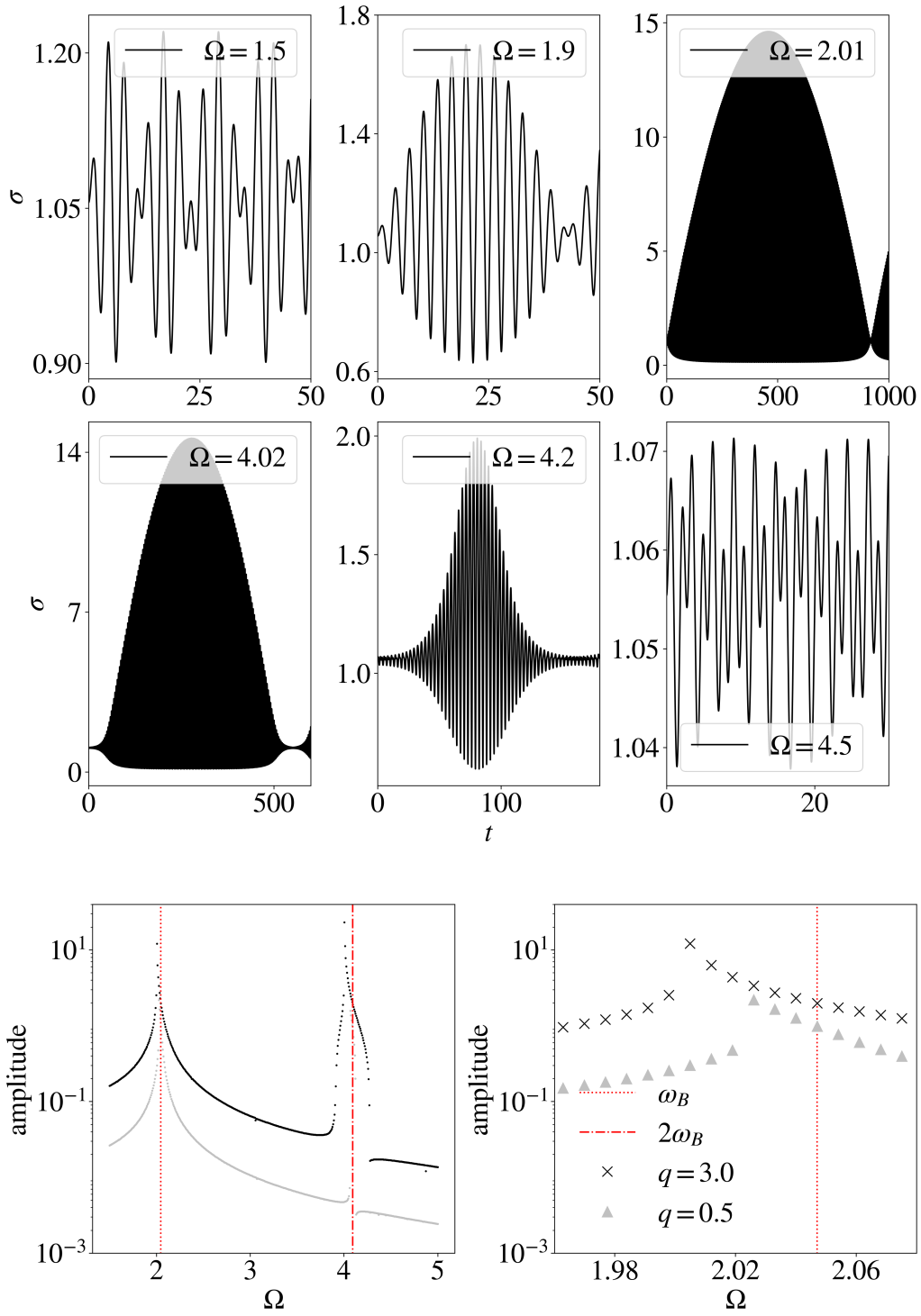

Figure 2.7: (upper) Radius dynamics whilst modulating the interaction strength U as $U(t) = p + q\cos(\Omega t)$, $p = 4.0, q = 3.0$ in three dimensions. (lower) Resonant amplitude $(\sigma_{min} - \sigma_{max})/2$ versus driving frequency Ω for $p = 4.0$, $q = 3.0, 0.5$. Resonance peaks occuring near undriven breathing frequency ω_B and harmonics as $2\omega_B/n$ (for integer n) with offset amplified by the magnitude of the driving force q.

Chapter 3

Numerical study of the Gross-Pitaevskii equation

3.1 Overview

In this chapter we will discuss the numerical methods used to treat the Gross-Pitaevskii equation numerically before providing some basic results regarding ground state wavefunctions and normal modes.

In section 3.2 we discuss the symplectic integration methods we will use to solve the GPE numerically. We will begin with some simpler first and second-order schemes in 3.2.1 and 3.2.2 before discussing the composition methods used for more efficient, higher order schemes in 3.2.3. We will then outline the process used to determine the sixth order *Runge-Kutta-Nyström* methods [25], which we will use in the remainder of our GPE analysis, in 3.2.4. Once we have determined the mechanisms for time evolution of the GPE, we will discuss the imaginary time propagation method for approximating ground state solutions to the GPE in section 3.3. We will provide a proof

of some features of the GPE in imaginary time in 3.3.2. Quantities of interest of the resulting wavefunctions are defined and sampling methods are discussed in section 3.4. We will then apply the imaginary time propagation method to investigate the ground state solutions of the GPE for a range of interaction strengths U in section 3.5. We will compare these ground state approximations to our variational ansätze and discuss the regimes of U, as well as the extent of the spatial region x, in which these ansätze are valid in 3.5.1. Finally, we will apply our numerical algorithms to compare the normal modes of the GPE with those of our variational equations in terms of their characteristic frequencies in 3.5.2.

3.2 Symplectic integrators and operator splitting

Symplectic integration schemes are numerical schemes used to solve Hamiltonian systems. For Hamilton's equations in canonical coordinates p and q we have the equations of motion (3.1)

$$\dot{p} = -\frac{\partial H}{\partial q} \quad , \quad \dot{q} = \frac{\partial H}{\partial p}. \tag{3.1}$$

Which may also be written in terms of a *symplectic matrix* as

$$\begin{pmatrix} \dot{p} \\ \dot{q} \end{pmatrix} = \begin{pmatrix} 0 & 1 \\ -1 & 0 \end{pmatrix} \begin{pmatrix} \frac{\partial H}{\partial p} \\ \frac{\partial H}{\partial q} \end{pmatrix}. \tag{3.2}$$

The time evolution of these equations $(p(t), q(t)) = \phi_t(p(t_0), q(t_0))$, is a symplectic map, meaning it conserves the differential 2-form $\omega = dp \wedge dq$. In classical mechanics, a symplectic map is a canonical transformation on the phase space which is volume preserving and preserves this 2-form ω. Any particular numerical scheme is considered symplectic if it also conserves this

2-form. For a more detailed discussion of this background see any of [64–66]. When solving Hamiltonian systems, symplectic integrators offer advantages over more traditional numerical schemes. In particular, in the current work we are interested in computing small energy differences between various interaction ramp variants. Finite difference methods, such as Runge-Kutta methods, often contains secular terms in the total energy truncation error. These terms lead to quadratic growth over long times and would therefore be unsuitable for our current purposes. The methods we present in this section exhibit near conservation of the total energy over long times at relatively large step sizes [67]. Additionally, symplectic methods have the benefit of being time reversible. This characteristic allows the composition of schemes to develop successively higher order schemes [23] as we see in 3.2.3.

A widely used class of symplectic integrators are centred around separable Hamiltonian systems, the GPE being an example of such a system. In the case of the GPE, splitting the equation into kinetic terms $\hat{A}$ and potential terms $\hat{B}$ allows either term to be solved analytically. The kinetic term is solved in frequency space, and the external potential and interaction terms in coordinate space. This operator splitting is referred to as a symplectic method as the resulting schemes preserve the phase space volume and the symplectic form ω.

3.2.1 First order symplectic integrators

Before discussing the more precise schemes which we use in our analysis, we first give a demonstrative example. Consider the GPE as the composition of two operators acting on a complex field ψ with one being a small perturbation

$$i\hbar\partial_t\psi = \left(\hat{A} + \epsilon\hat{B}\right)\psi \tag{3.3}$$

, with ϵ being some small parameter $\epsilon \in \mathbb{R}$. This system has a formal solution, although not in closed form, as the complex exponential

$$\psi(\mathbf{x}, dt) = \exp\Big(-idt(\hat{A} + \epsilon\hat{B})/\hbar\Big)\psi(\mathbf{x}, 0). \tag{3.4}$$

As the quantities $\hat{A}$ and $\hat{B}$ are operators, they will not generally commute. However, if we were to expand the above exponential in terms of the Baker-Campbell-Hausdorff formula we would see that treating them as if they do leads to an error of order dt^2 as

$$\psi(\mathbf{x}, dt) = \Big(\exp\Big(-idt\hat{A}/\hbar\Big)\exp\Big(-idt\epsilon\hat{B}/\hbar\Big) + \mathcal{O}(dt^2)\Big)\,\psi(\mathbf{x}, 0). \tag{3.5}$$

The elimination of these higher order terms in a Baker–Campbell–Hausdorff expansion is the purpose of symplectic integration schemes.

3.2.2 Symplectic integrators of order two

Consider two operators $\hat{A}$ and $\hat{B}$ with a non-zero commutator and some small real number τ representing the step size. The question of the correct manner in which to take these alternating steps in frequency and coordinate space can be framed as such.

Find a set of real numbers $(a_1, a_2, ..., a_k)$ and $(b_1, b_2, ..., b_k)$ such that for a given integer n called the order of the integrator the following relation holds:

$$\exp\Big(\tau\left(\hat{A} + \hat{B}\right)\Big) = \prod_{i=1}^{k} \exp\Big(a_i\tau\hat{A}\Big)\exp\Big(b_i\tau\hat{B}\Big) + \mathcal{O}(\tau^{n+1}). \tag{3.6}$$

When this equation is solved for a desired order n, the parameters $\{a_i, b_i\}$ will, when implemented numerically, yield a solution to the exponential $\exp\Big(\tau(\hat{A} + \hat{B})\Big)$ with leading error term $\mathcal{O}(\tau^{n+1})$.

The typical approach to calculating $\{a_i, b_i\}$ combinations, which is detailed

in [21], is to expand the above equation to the desired order n as below. Then after pairing off coefficients of operator permutations $\hat{A}$, $\hat{B}$, $\hat{A}\hat{B}$, $\hat{B}\hat{A}$... and so on, we find

$$\exp\Big(\tau\left(\hat{A}+\hat{B}\right)\Big) = 1+\tau(\hat{A}+\hat{B})+\frac{1}{2}\tau^2(\hat{A}+\hat{B})^2+... \tag{3.7}$$

$$\prod_i^k \exp\Big(a_i\tau\hat{A}\Big)\exp\Big(b_i\tau\hat{B}\Big) =$$

$$1+\tau(p_1\hat{A}+p_2\hat{B})+\tau^2(p_3\hat{A}\hat{B}+p_4\hat{B}\hat{A}+p_5\hat{A}^2+p_6\hat{B}^2)+... \tag{3.8}$$

, where p_i are polynomials in the parameters a_i and b_i proportional to the terms $\hat{A}$, $\hat{B}$, $\hat{A}\hat{B}$, $\hat{B}\hat{A}$ etc. Coefficients of like terms in (3.7) and (3.8) are then equated to give a system of equations for the parameters $\{a_i, b_i\}$. For example, for a first order integrator we would have

$$1+\tau(\hat{A}+\hat{B}) = 1+\tau(p_1\hat{A}+p_2\hat{B}). \tag{3.9}$$

Therefore, when we equate like terms here we find $p_1 = 1$ and $p_2 = 1$. The simplest solution to this would then be $k = 1$ or $p_1 = a_1$, $p_2 = b_1$, meaning we recover the proposed first order method equation (3.5) with $a_1 = b_1 = 1$ and the basic first order symplectic scheme S_1^1 (S_k^n being a symplectic scheme with k applications of exponential operators $e^{\tau\hat{A}}$ and $e^{\tau\hat{B}}$ and of order n),

$$S_1^1 = \exp\Big(\tau\hat{A}\Big)\exp\Big(\tau\hat{B}\Big). \tag{3.10}$$

By this approach a second order integrator can be found. By including terms of order τ^2 in equation (3.7) and (3.8) we find an additional equation for the parameters a_i, b_i proportional to $\hat{A}\hat{B}$ along with those found for the first

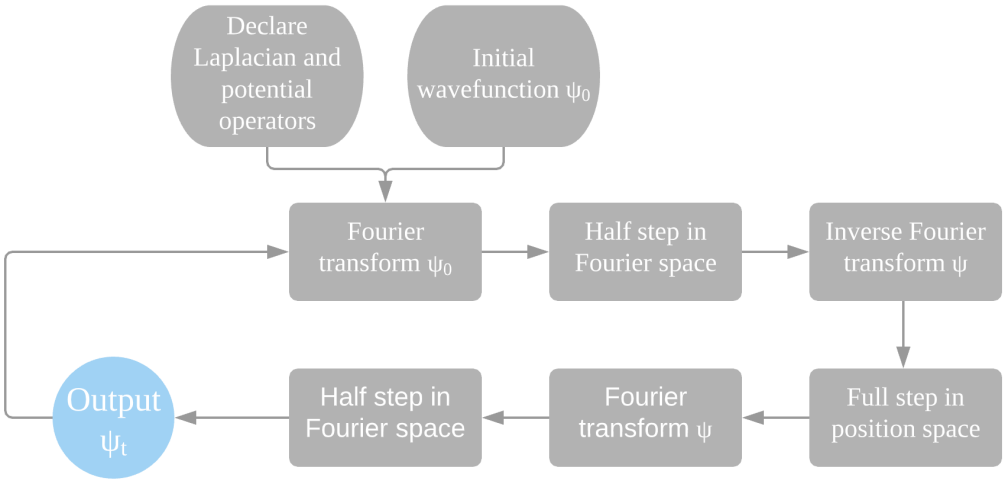

Figure 3.1: Flow diagram for Störmer-Verlet symplectic method with time step τ.

order terms,

$$a_1 (b_1 + b_2 + ... + b_k) + a_2 (b_2 + ... + b_k) + ... + a_k b_k = 1/2, \tag{3.11}$$

$$a_1 + a_2 + ... + a_k = 1, \tag{3.12}$$

$$b_1 + b_2 + ... + b_k = 1. \tag{3.13}$$

When solved with $k = 2$ this additional equation allows us to compute the canonical example amongst symplectic integrators, the Stormer-Verlet, or Leapfrog scheme [22, 23] with $a_1 = a_2 = 1/2$, $b_1 = 1$ and $b_2 = 0$

$$S_2^2(\tau) = \exp\left(1/2\tau\hat{A}\right) \exp\left(\tau\hat{B}\right) \exp\left(1/2\tau\hat{A}\right). \tag{3.14}$$

Implemented numerically this algorithm would follow the flow diagram figure 3.1.

3.2.3 Composition methods for symplectic integrators $n \geq 4$

Although it is technically possible to find higher order methods using the methods described above, it quickly becomes cumbersome to solve the ensuing systems of equations. Following the process discussed in [21] and [23], it is suggested that an integrator of order $n+2$ can be formed by symmetric repetition of an order n integrator as

$$S^4(\tau) := S^2(x_1\tau)S^2(x_0\tau)S^2(x_1\tau). \tag{3.15}$$

We take the second-order Stormer-Verlet scheme equation 3.14 as an example,

$$S_2^2(\tau) = \exp\Big(\frac{1}{2}\tau\hat{A}\Big)\exp\Big(\tau\hat{B}\Big)\exp\Big(\frac{1}{2}\tau\hat{A}\Big). \tag{3.16}$$

By applying the Baker-Campbell-Hausdorff formula successively we can write $S_2^2(\tau)$ as a single exponential. Consider some arbitrary operators $\hat{X}$ and $\hat{Y}$. The Baker-Campbell-Hausdorff formula tells us

$$\ln(e^{\hat{X}}e^{\hat{Y}}) = \hat{X} + \hat{Y} + \frac{1}{2}[\hat{X}, \hat{Y}] + ... \tag{3.17}$$

We want to know the equivalent of this expansion for the expression $e^{\hat{X}}e^{\hat{Y}}e^{\hat{X}}$. We define an additional operator $\hat{Y}' = \frac{1}{2}\hat{Y}$. The product of three exponentials can then be written as

$$e^{\hat{X}}e^{\hat{Y}}e^{\hat{X}} = e^{\hat{X}}e^{\hat{Y}'}e^{\hat{Y}'}e^{\hat{X}}. \tag{3.18}$$

If we define the resulting operator $\hat{W}$ as $e^{\hat{X}}e^{\hat{Y}}e^{\hat{X}} = e^{\hat{W}}$ then by successive application of the Baker–Campbell–Hausdorff we would have

$$\hat{W} = (\hat{X} + 1/2\hat{Y} + ...) + (1/2\hat{Y} + \hat{X} + ...) = 2\hat{X} + \hat{Y} + ... \tag{3.19}$$

Where we have restricted ourselves to terms linear in $\hat{X}$ and $\hat{Y}$ for brevity's sake. A more comprehensive expression is given by [21] as

$$\begin{aligned}\hat{W} =& 2\hat{X} + \hat{Y} + \frac{1}{6}[\hat{Y},[\hat{Y},\hat{X}]] - \frac{1}{6}[\hat{X},[\hat{X},\hat{Y}]] \\ &+ \frac{7}{360}[\hat{X},[\hat{X},[\hat{X},[\hat{X},\hat{Y}]]]] - \frac{1}{360}[\hat{Y},[\hat{Y},[\hat{Y},[\hat{Y},\hat{X}]]]] \\ &+ \frac{1}{90}[\hat{X},[\hat{Y},[\hat{Y},[\hat{Y},\hat{X}]]]] + \frac{1}{45}[\hat{Y},[\hat{X},[\hat{X},[\hat{X},\hat{Y}]]]] \\ &- \frac{1}{60}[\hat{X},[\hat{X},[\hat{Y},[\hat{Y},\hat{X}]]]] + \frac{1}{30}[\hat{Y},[\hat{Y},[\hat{X},[\hat{X},\hat{Y}]]]] + ...\end{aligned} \tag{3.20}$$

If we apply this expression to the Stormer-Verlet scheme equation (3.16) we find

$$\begin{aligned}S_2^2(x\tau) =& \exp\Big(x\tau(\hat{A}+\hat{B}) + \frac{1}{12}x^3\tau^3[\hat{B},[\hat{B},\hat{A}]] \\ &- \frac{1}{24}x^3\tau^3[\hat{A},[\hat{A},\hat{B}]] + \frac{7}{5760}x^5\tau^5[\hat{A},[\hat{A},[\hat{A},\hat{B}]]] + ...\Big).\end{aligned} \tag{3.21}$$

Which after once again applying (3.20) in the spirit of (3.15) yields the fourth-order scheme S_4^4:

$$\begin{aligned}S_4^4(\tau) =& S_2^2(x_1\tau)S_2^2(x_0\tau)S_2^2(x_1\tau) &(3.22)\\ =& \exp\Big(\tau\alpha_1(2x_1+x_0) + \tau^3\alpha_2(2x_1^3+x_0^3) + ...\Big) &(3.23)\end{aligned}$$

, where the terms α_i are defined for notational convenience as $\alpha_1 = (\hat{A} + \hat{B}), \alpha_2 = \frac{1}{12}[\hat{B},[\hat{B},\hat{A}]]$ etc. We can solve for x_0 and x_1 by requiring $S_4(\tau) = \exp\Big(\tau(\hat{A+B})\Big) + \mathcal{O}(\tau^{n+1})$. This requirement leads to the system of equations $2x_1 + x_0 = 1$ and $2x_1^3 + x_0^3 = 0$ with solutions

$$\begin{aligned}x_0 = -\frac{2^{1/3}}{2-2^{1/3}} \quad , \quad x_1 = \frac{1}{2-2^{1/3}} &(3.24)\\ \approx -1.70241 \quad , \quad \approx 1.35121. &(3.25)\end{aligned}$$

Therefore, the full form of a fourth-order symplectic scheme is

$$S_4^4(\tau) = \exp\Big(a_1\tau\hat{A}\Big)\exp\Big(b_1\tau\hat{B}\Big) \times ... \times \exp\Big(a_4\tau\hat{A}\Big) \tag{3.26}$$

, with coefficients $a_1 = a_4 = 1/2x_1$, $b_1 = b_3 = x_1$, $b_2 = x_0$, and $a_2 = a_3 = 1/2(x_0 + x_1)$.

In this manner we can successively develop symplectic schemes of order $n+2$ by concatenating three instances of an order n scheme and solving for the parameters a_i and b_i.

3.2.4 Symplectic Runge-Kutta-Nyström schemes of order $n = 6$

Many possible schemes can be constructed using the composition methods above. Several of which ranging from order $n = 2$ to $n = 8$ are presented in [24] with extensive analysis of the performance of each. Amongst the best performing schemes discussed are the sixth-order Runge-Kutta-Nyström (SRKN) schemes [25] which we present here shortly. These SRKN methods are formed by symmetric compositions of operators $\exp\left(a_i\tau\hat{A}\right)$ and $\exp\left(b_i\tau\hat{B}\right)$. Since the operators $\hat{A}$ and $\hat{B}$ are qualitatively different, there are two possible compositions to be considered. Schemes beginning and ending with an application of the $\hat{A}$ exponential:

$$SRKN_s^a = \exp\left(a_1\tau\hat{A}\right)\exp\left(b_1\tau\hat{B}\right) \times ... \times \exp\left(b_s\tau\hat{B}\right)\exp\left(a_{s+1}\tau\hat{A}\right) \quad (3.27)$$

, where $a_{s+2-i} = a_i$ and $b_{s+1-i} = b_i$. Or schemes beginning and ending with an application of the $\hat{B}$ exponential:

$$SRKN_s^b = \exp\left(b_1\tau\hat{B}\right)\exp\left(a_1\tau\hat{A}\right) \times ... \times \exp\left(a_s\tau\hat{A}\right)\exp\left(b_{s+1}\tau\hat{B}\right) \quad (3.28)$$

, where $a_{s+1-i} = a_i$ and $b_{s+2-i} = b_i$.

Both of these methods of composition require s evaluations of $e^{\hat{A}}$ and $e^{\hat{B}}$. Rather than computing the coefficients a_i and b_i by solving systems of equations or compositions of lower order schemes, [25] treats the process of finding

these schemes as an optimisation problem. An objective function based on the coefficients $\{a_i, b_i\}$ in (3.27) and (3.28) is minimised numerically. Choices of initial coefficients were generated at random until 10,000 local minima of the objective function were found. These 10,000 candidates were then analysed further using a range of sample problems (one of which includes the non linear Schrödinger equation). Two schemes of order 6 found using this method are shown below and unless stated otherwise will be used for all numerical integration calculations in the rest of this thesis.

$$\begin{aligned} SRKN_{11}^{b}(\tau) = &\exp\Big(b_1\tau\hat{B}\Big)\exp\Big(a_1\tau\hat{A}\Big)\times ...\times \exp\Big(b_5\tau\hat{B}\Big)\exp\Big(a_5\tau\hat{A}\Big)\exp\Big(b_6\tau\hat{B}\Big) \\ &\times \exp\Big(a_5\tau\hat{A}\Big)\exp\Big(b_5\tau\hat{B}\Big)\times ...\times \exp\Big(a_1\tau\hat{A}\Big)\exp\Big(b_1\tau\hat{B}\Big) \end{aligned} \tag{3.29}$$

$$\begin{aligned} SRKN_{14}^{a}(\tau) = &\exp\Big(a_1\tau\hat{A}\Big)\exp\Big(b_1\tau\hat{B}\Big)\times ...\times \exp\Big(a_7\tau\hat{A}\Big)\exp\Big(b_7\tau\hat{B}\Big)\exp\Big(a_8\tau\hat{A}\Big) \\ &\times \exp\Big(b_7\tau\hat{B}\Big)\exp\Big(a_7\tau\hat{A}\Big)\times ...\times \exp\Big(b_1\tau\hat{B}\Big)\exp\Big(a_1\tau\hat{A}\Big) \end{aligned} \tag{3.30}$$

The coefficients for both schemes are given in tables 3.1 and 3.2.

3.3 Ground states of the time independent Gross-Pitaevskii equation

In this section, we will discuss the method of approximating ground state solutions to Schrödinger like equations via imaginary time propagation.

3.3.1 Schrödinger equations in imaginary time

As an extension of the Schrödinger equation, the ground state wavefunctions of the GPE can be computed to arbitrary precision using the method of

a_1	0.0378593198406116	b_1	0.09171915262446165
a_2	0.102635633102435	b_2	0.183983170005006
a_3	0.0258678882665587	b_3	0.05653436583288827
a_4	0.314241403071447	b_4	0.004914688774712854
a_5	0.130144459517415	b_5	0.143761127168358
a_6	0.106417700369543	b_6	0.328567693746804
a_7	0.00879424312851058	b_7	$1/2 - (b_1 + ... + b_6)$
a_8	$1 - 2(a_1 + ... + a_7)$		

Table 3.1: Coefficients of the $SRKN_{14}^{a}$ scheme.

a_1	0.123229775946271	b_1	0.0414649985182624
a_2	0.290553797799558	b_2	0.198128671918067
a_3	-0.127049212625417	b_3	-0.0400061921041533
a_4	-0.246331761062075	b_4	0.0752539843015807
a_5	0.357208872795928	b_5	-0.0115113874206879
		b_6	$\frac{1}{2} - (b1 + ... + b5)$

Table 3.2: Coefficients of the $SRKN_{11}^{b}$ scheme.

imaginary time propagation. This method consists of a Wick rotation in time from t to it. Consider any Schrödinger type equation transformed into imaginary time

$$\partial_{it}\psi = -H\psi/\hbar. \tag{3.31}$$

Decompose the wavefunction ψ as a sum of the energy eigenfunctions ϕ_i as

$$\psi = \sum_i c_i \cdot \phi_i. \tag{3.32}$$

For each individual eigenfunction the solution to (3.31) becomes

$$\phi_i(\tau) = e^{-\tau E_i}\phi_i(0) \tag{3.33}$$

, where we have defined the imaginary time parameter τ as $\tau \stackrel{\text{def}}{=} it/\hbar$. The solution for the full wavefunction is then the sum over all eigenfunctions ϕ_i where

$$\psi(\tau) = \sum_i e^{-\tau E_i} c_i \cdot \phi_i(0). \tag{3.34}$$

Which means at every step of size τ, the relative population of the ground state eigenstate to that of all other states is proportional to the energy of said eigenstate as

$$\frac{\phi_i(\tau)}{\phi_0(\tau)} = e^{-\tau(E_i - E_0)} \frac{\phi_i(0)}{\phi_0(0)}. \tag{3.35}$$

Meaning if this process is repeated many times, the overall wavefunction ψ will tend towards the ground state ϕ_0 as long as the initial state $\psi(0)$ has some finite overlap with the ground state ϕ_0.

3.3.2 Normalisation and energy decay in the GPE

Here we provide a proof of some features of the imaginary time propagation method in the Gross-Pitaevskii equation [26]. Firstly, consider the GPE transformed to imaginary time ie. $t \to \tau = it$:

$$\partial_\tau \psi = \frac{1}{2}\nabla^2\psi - V(\mathbf{x})\psi - U|\psi|^2\psi, \quad \tau > 0, \mathbf{x} \in \Omega, \tag{3.36}$$

$$\psi(\mathbf{x}, 0) = \psi_0(\mathbf{x}), \quad \mathbf{x} \in \Omega, \tag{3.37}$$

$$\psi(\mathbf{x}, \tau) = 0, \quad \mathbf{x} \in \Gamma, \tau \geq 0 \tag{3.38}$$

, where $\Omega \subset \mathbb{R}^D$, $V(\mathbf{x})$ is the trapping potential and $\Gamma = \partial\Omega$ is the boundary of the region Ω.

We can then establish the following theorem.

Theorem 2. *Suppose* $V(\boldsymbol{x}) \geq 0$ *for all* $\boldsymbol{x} \in \Omega$, $U \geq 0$, $\quad 0 < \tau < \tau' < \infty$

and $||\psi_0|| = 1$*, then*

$$(i) \quad ||\psi(\boldsymbol{x}, \tau')|| \leq ||\psi(\boldsymbol{x}, \tau)|| = 1, \tag{3.39}$$

$$(ii) \quad E\left[\psi(\boldsymbol{x}, \tau')\right] \leq E\left[\psi(\boldsymbol{x}, \tau)\right] \tag{3.40}$$

, where we have adopted the norm $||\cdot||$ *as* $||\cdot||_{L^2(\Omega)}$*.*

Proof. To prove (i), we compute the time derivative of $||\psi||$, using (3.36) and integrating by parts we find

$$\frac{d}{d\tau}||\psi|| = \int_\Omega \left(\dot{\psi}\psi^*\right) d\mathbf{x} + \text{h.c.} \tag{3.41}$$

$$= \int_\Omega \left[\frac{1}{2}\psi^*\nabla^2\psi - V(\mathbf{x})|\psi|^2 - U|\psi|^4\right] dx + \text{h.c.} \tag{3.42}$$

$$= -2\int_\Omega \left[\frac{1}{2}|\nabla\psi|^2 + V(\mathbf{x})|\psi|^2 + U|\psi|^4\right] dx \leq 0 \tag{3.43}$$

, which implies 2 (i).

To prove (ii) we use (2.15) along with (3.36) as

$$\frac{d}{d\tau}E[\psi] = \frac{d}{d\tau}\int_\Omega \frac{1}{2}|\nabla\psi|^2 + V(\mathbf{x})|\psi|^2 + \frac{U}{2}|\psi|^4 d\mathbf{x} \tag{3.44}$$

$$= \int_\Omega \dot{\psi}\left(-\frac{1}{2}\nabla^2 + V(\mathbf{x}) + U|\psi|^2\right)\psi^* d\mathbf{x} + \text{h.c.} \tag{3.45}$$

$$= \int_\Omega -\left|\frac{1}{2}\nabla^2 - V(\mathbf{x}) - U|\psi|^2\right|^2 d\mathbf{x} + \text{h.c} = -2\int_\Omega |\partial_\tau\psi|^2 d\mathbf{x} \tag{3.46}$$

, which implies (ii).

□

It should be noted here that, even though we stated all numerical calculations would be performed using the $SRKN$ methods defined in the previous section, imaginary time propagation calculations are the exception. A single time step taken in imaginary time τ using these 6^{th} order methods reduces the norm $||\psi||$ by such an amount that the 64 bit floating point array of ψ is rounded to zero. For this reason, any use of the imaginary time propagation algorithm will use the 4^{th} order symplectic scheme equation (3.26)

3.4 Energy and Variance of the time-dependent Gross-Pitaevskii equation

To record excess energy after various ramps in Chapter 4 we will be taking the difference between the final energy and the ground state energy. Since these differences will at times reach values of the order 10^{-10} and smaller, we will require measurements of energy with a precision at least greater than these minimal values. To reach these high levels of precision we use higher order central difference methods to approximate the GPE energy functional (2.15). As a reminder, the GPE energy functional is

$$E[\psi(\mathbf{x},t)] = \int_\Omega d\mathbf{x} \frac{\hbar^2}{2m}|\nabla\psi|^2 + V(\mathbf{x})|\psi|^2 + \frac{U}{2}|\psi|^4. \tag{3.47}$$

The external potential and interaction terms can be solved exactly (up to spatial discretisation error) using the wavefunction. The kinetic energy term will be discretised using the methods below.

3.4.1 Central difference methods

Consider the Taylor series of some arbitrary function $f(x+h)$ plus some small deviation h

$$f(x+h) = f(x) + hf'(x) + h^2\frac{f''(x)}{2!} + ... \tag{3.48}$$

Rearranging this, we can find the common $\mathcal{O}(h)$ approximation to the derivative $f'(x)$

$$\frac{f(x+h)-f(x)}{h} = f'(x) + h\frac{f''(x)}{2!}. \tag{3.49}$$

∇^n	Order	-4	-3	-2	-1	0	1	2	3	4
1	2				-1/2	0	1/2			
	4			1/12	-2/3	0	2/3	-1/12		
	6		-1/60	3/20	-3/4	0	3/4	-3/20	1/60	
	8	1/280	-4/105	1/5	-4/5	0	4/5	-1/5	4/105	-1/280

Table 3.3: Table of central difference coefficients for first derivatives.

By the same process, various higher order central difference approximations to the derivative can be formed. Table 3.3 shows the coefficients of these higher order central difference schemes, for example, the second-order approximation to the first derivative has coefficients $-1/2, 0$ and $1/2$ meaning the derivative would be:

$$\frac{f(x+h) - f(x-h)}{2h} = f(x) + h^2 \frac{(f'''(x_1) + f'''(x_2))}{12} \tag{3.50}$$

In all numerical calculations for the GPE energy, we use the 8^{th} order central difference of table 3.3 in the interior of $\psi(\mathbf{x})$. Around the boundaries of $\psi(\mathbf{x})$ we use successively lower order schemes until at the boundary $\psi(\partial\mathbf{x})$ we use forward or backward derivatives before integrating.

3.4.2 Wavefunction variances and variational equation comparisons

The width of the wavefunction $\psi(\mathbf{x}, t)$ is measured using the variance $\mathrm{Var}[|\psi|^2]$ given by

$$\mathrm{Var}[|\psi|^2] = \int_{\mathbf{x}} (x - \langle x \rangle)^2 |\psi|^2 dx = \langle x^2 \rangle - \langle x \rangle^2. \tag{3.51}$$

However, as the mean $\langle x \rangle$ is zero when no dipole mode is present, in our analysis this will usually reduce to the width r_{GP}

$$r_{GP} = \int_{\Omega} \mathbf{x}^2 |\psi|^2 d\mathbf{x}. \tag{3.52}$$

To have some commensurable quantity between the GPE and the two variational equations, we compute r_{VM} for each of the two variational ansätze. This leads to rescaled versions of the variational parameters σ and ρ to be compared to the GPE data

$$r_G = \frac{\sigma^2}{2} \quad , \quad r_{TF} = \frac{\rho^2}{5} \tag{3.53}$$

, for the widths of the Gaussian ansatz r_G and the Thomas-Fermi ansatz r_{TF}.

3.5 Numerical solutions of the one dimensional GPE

In this section, we will implement the numerical methods outlined in the beginning of this chapter. Initially in 3.5.1 we will calculate the ground state wavefunctions necessary for performing an analysis of interaction ramps. This will be performed using the imaginary time propagation methods discussed previously.

We will take some time to analyse how these ground states respond to varying interaction strength as well as the regimes of U satisfying either of the Gaussian and Thomas-Fermi ansätze. We will then compare the characteristics of GPE dynamics to those predicted by the variational equations in 3.5.2, namely the frequencies of breathing modes versus interaction strength. Finally, we will show the effect or lack thereof of the interaction strength on the dipole mode frequency.

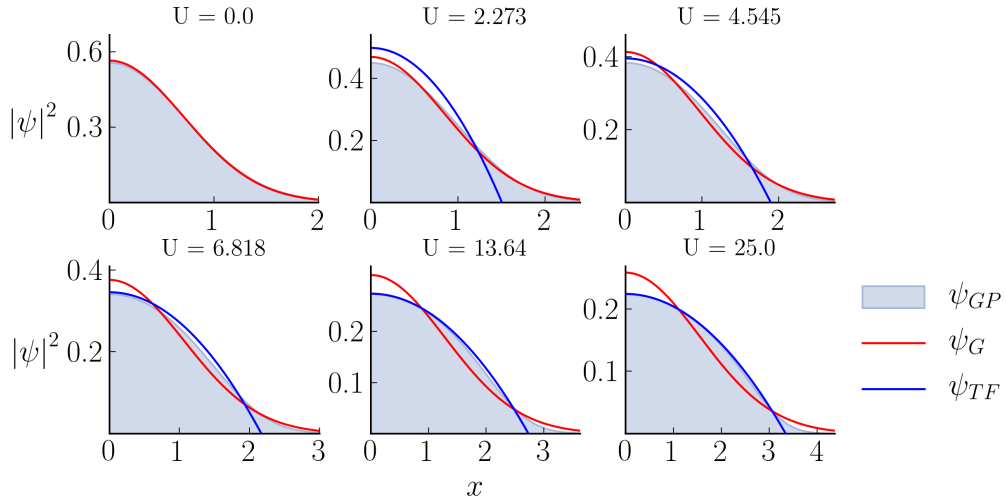

Figure 3.2: GPE ground state wavefunctions as compared to the Thomas-Fermi and Gaussian variational ansätze. Parameters for ground state calculations: $m = 10$, $\epsilon = 10^{-10}$, $n = 25$, initial time step $d\tau = 0.5$, and spatial discretisation $dx = 0.025$.

3.5.1 Gross-Pitaevskii ground states

The imaginary time propagation method allows us to calculate ground state wavefunctions of the GPE to arbitrary precision for any value of the interaction strength U. However, the precision achievable is heavily dependent on the discretisation used. At too large an imaginary time step size $d\tau$, the algorithm will plateau at high energy states. To reach an approximation to the ground state of sufficient precision for our purposes, we are then forced to use very fine discretisations in time. Of course using such a small time step will quickly become tiresome, so instead we use an *adaptive* imaginary time step $d\tau$, decreasing as the evolution goes on. The criteria we use be to reduce the step by a factor of $1/2$ if a plateau in the value of previous energy measurements is detected. A plateau will be defined as a sequence of energy samples satisfying $\text{abs}(E_i/E_{i-m}) > 1 - \epsilon$ for some integer m and

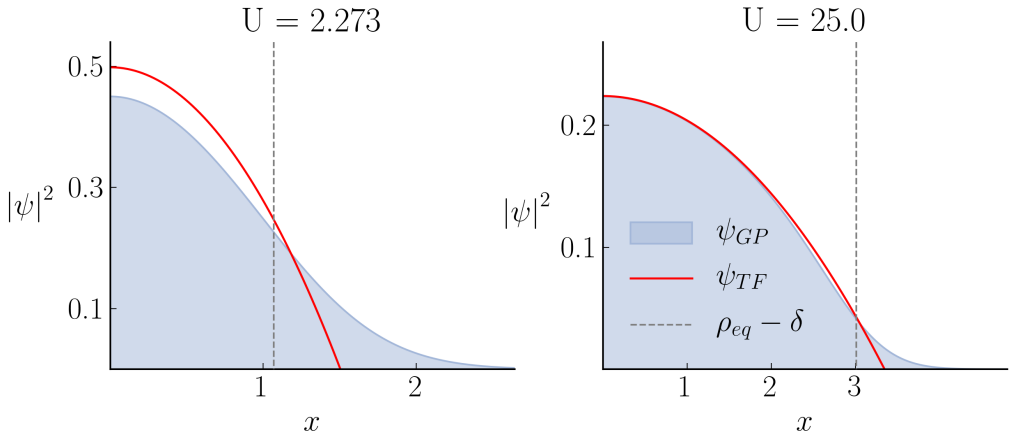

Figure 3.3: Particles inserted to the right of the dotted line would have more kinetic than potential energy meaning the Thomas-Fermi approximation is only valid in the region to the left of this line.

small parameter ϵ and each loop will halted after some fixed number of steps n.

An initial comparison of the GPE and variational ground state solutions shows clearly the areas in which either variational ansatz is valid. Figure 3.2 shows the ground state solutions (using parameters $m = 10$, $\epsilon = 10^{-10}$, $n = 25$) versus the stationary solutions of Gaussian isotropic and Thomas-Fermi variational equations (2.37) and (2.49) respectively. In the limit of the non-interacting GPE, the Gaussian ansatz is the exact solution by design, however the Thomas-Fermi solution is undefined. As the strength of interactions grow, the inverted parabola form of the Thomas-Fermi solution becomes a much stronger approximation to the GPE solution.

At the boundary of the condensate the assumption that the potential dominates over the kinetic energy fails. We can see the point at which the crossover between kinetically dominated and potentially dominated energy contributions occurs as follows. The wavefunction density in the one dimen-

sional Thomas-Fermi regime is $|\psi(x)|^2 = (\mu - V(x))/U$. By expanding the wavefunction about some point $x = \rho$ at the boundary of the condensate, this radial component becomes

$$|\psi(x)|^2 = \frac{\mu - V(\rho)}{U} - \frac{\partial_x V(x)\Big|_\rho \cdot (x-\rho)}{U}$$
$$\Rightarrow \psi(x) = \left(\frac{F \cdot (x-\rho)}{U}\right)^{1/2} \tag{3.54}$$

, where F is the force exerted on a particle at the boundary of the condensate due to an isotropic harmonic potential. We also use the fact that $\mu - V(x) = 0$ when evaluated at the boundary $x = \rho$. When we assume $V(x)$ is a harmonic potential the force F is

$$F = -\nabla V(\rho) = -m\omega^2\rho \tag{3.55}$$

, where the minus sign implies the force is acting towards the centre of the trap. The kinetic energy per particle of a condensate satisfying (3.54) is

$$\frac{\hbar^2}{2m}\frac{\left|\frac{d}{dx}\psi\right|^2}{|\psi|^2} \sim \frac{\hbar^2}{8m(\rho - x)^2}. \tag{3.56}$$

In the Thomas-Fermi regime, we assume that the wavefunction density vanishes at some width ρ which then implies that $\mu - V(\rho) = 0$. We can then make a linear approximation to this difference in the bulk of the condensate and say

$$\mu - V(x) = |F|(\rho - x) \tag{3.57}$$

, where $|F|$ is the magnitude of the force F. The crossover point at which the energy contributions due to the kinetic energy of particles becomes greater than that of the potential energy occurs when $\delta \approx \rho - x$ for

$$\delta = \left(\frac{\hbar^2}{8m^2\omega^2\rho}\right)^{1/3}. \tag{3.58}$$

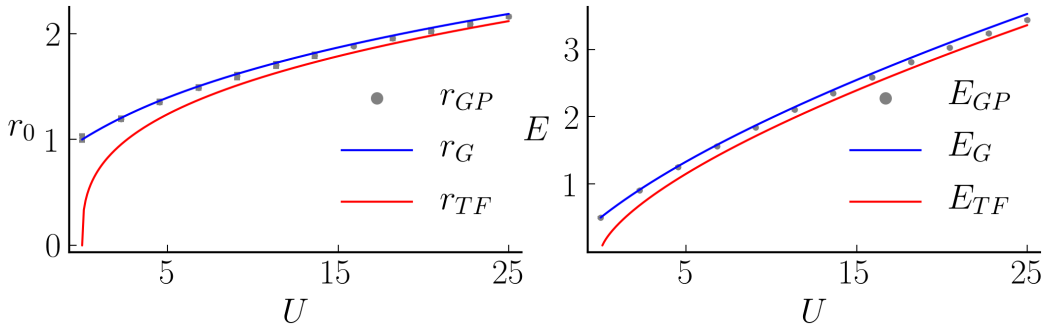

Figure 3.4: Widths $\int_x x^2|\psi|^2 dx$ and energies $E[\psi]$ of ground states from GPE, Gaussian and Thomas-Fermi variational equations. GPE errors calculated from the amplitude of residual oscillations after imaginary time propagation is halted for the r_0 data and the square of said oscillations for the E_0 data.

The parameter δ gives us an idea of the region of the condensate wavefunction in which the Thomas-Fermi approximation makes a reasonably good prediction of the true GPE solution. Comparing to the numerical results once again, in figure 3.3 we see that the region within this boundary δ, ie. the proportion of particles within the condensate satisfying the Thomas-Fermi condition, grows larger as we increase the interaction strength in the system as expected. Further discussion of this result and other features of the surface structure of BEC's in the Thomas Fermi regime can be found in [68].

3.5.2 Normal modes of the GPE

In Chapter 2, we studied the monopole and quadrupole normal modes of a BEC using our variational equations of motion for a three-dimensional condensate. In one-dimensional systems, the scope of possible dynamical modes is restricted to monopole and dipole modes. Here we compare the

breathing mode dynamics of the GPE with that of the Gaussian and Thomas-Fermi variational equations. We also sample the frequency of the dipole mode for the GPE alone.

Breathing modes

To initiate dynamics from the calculated ground states, we apply a sudden quench in U. If starting from a ground state ψ_0 at some value U_i, U is varied to some final value U_f rapidly, forcing the system into a breathing mode with frequency ω_B. An example of this effect is provided in figure 3.5. We then use an FFT to convert the $r(t)$ signal into its frequency domain representation. The dominant Fourier mode in this representation is the breathing mode. By sampling these dominant frequencies we can confirm the results found in Chapter 2 for isotropic breathing frequencies, namely the $\sqrt{D+2}$ limit at large U and $\omega = 2$ for the noninteracting limit. In the intermediate range we find a good agreement between the simplified Gaussian ansatz and the full GPE calculation for the frequency of breathing modes.

We note that finite size effects have a notable effect on the values measured for any characteristic frequencies. In this section as well as the following section, the error ranges for both ω_B and ω_D are calculated as follows. We calculate three versions of $\sigma(t)$ or $\mu(t)$ data using different discretisation schemes. Once using a control discretisation of (dx_1, dt_1), then two more with finer steps in space and time (dx_2, dt_1) and (dx_1, dt_2). We record the deviations between these three calculations, taking the maximum difference to be an upper bound on the numerical error. Discretisations used for the data shown in 3.6 are, in pairs,
$(dx, dt) = \{(0.025, 0.05), (0.025, 0.025), (0.0125, 0.05)\}$.

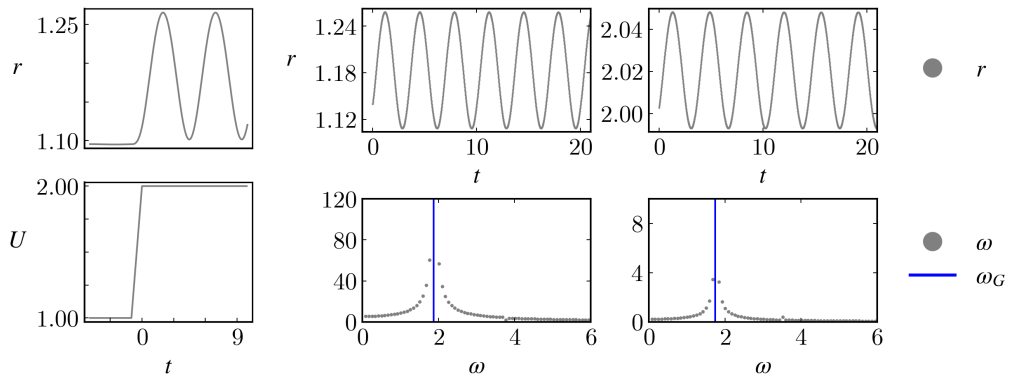

Figure 3.5: (left) Breathing mode induced by a rapid quench in U from $U = 1$ to $U = 2$. (centre & right) Fourier analysis for (centre) $U = 2$ and (right) $U = 20$ breathing mode (arbitrary y-axis units).

Dipole modes

Additionally, in the full GPE we can also investigate dipole type oscillations, a phenomenon we did not allow for in our variational ansätze. In a three dimensional condensate there are three available dipole modes, one for each Cartesian axis. In the one-dimensional system there is only one. Dipole motion is investigated by tracking the mean of the wavefunction $\mu(t) = \int_x \mathbf{x}|\psi(\mathbf{x},t)|^2 d\mathbf{x}$. When dipole oscillations are initiated (by offsetting the calculated ground states from the centre of the trap), we find that varying the internal interaction strength of the system has no effect on the frequency of the dipole mode (up to numerical discretisation error).
This result can be shown to be related to the Kohn theorem [69] as well as the generalised Ehrenfest theorem for the non-linear Scrödinger equation [70,71]. This constant frequency has been used as an indicator for calibration in experimental investigations into trapped BEC's [72]. The connection to trapped Bose gases has been discussed in detail in [73]

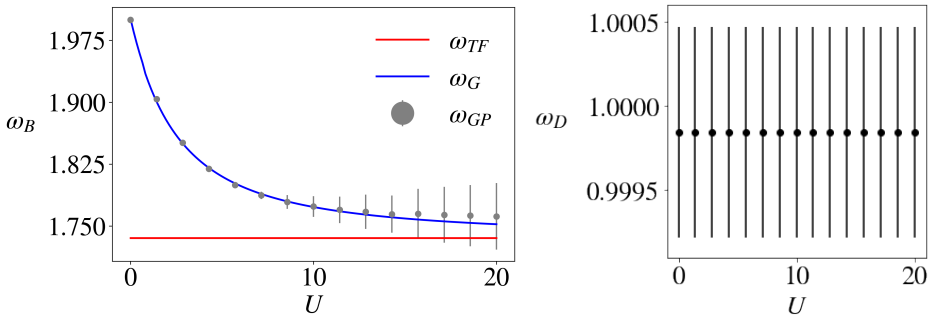

(a) (b)

Figure 3.6: **(a)** Breathing frequency ω_B from the GPE and both variational equations. **(b)** Constant dipole frequency from the GPE, errors approximated by three calculations over differing discretisations.

Chapter 4

Shortcuts to adiabaticity

4.1 Overview

In this chapter we will use the inverse engineering method discussed in section 1.2.3 to determine a number of interaction ramps approximating shortcuts to adiabaticity. We will briefly make some analytic arguments towards the behaviour of a BEC undergoing these ramps. Following this we will make a more thorough numerical investigation into their function.

The chapter will be split into three main sections. In section 4.2 we will implement the inverse engineering method used to derive an interaction ramp in a BEC. In general, this method will approximate a shortcut to adiabaticity in a BEC described by our variational approximations. We will refer to ramps designed in this way as *manufactured ramps*. We note 3 possible ramp variants but will largely focus on one manufactured ramp using a Thomas-Fermi-esque approximation to the Gaussian variational equation. In 4.2.4 we define the deviation between the final energy attained after the ramp and the ground state energy of the final target state as the function $\mathcal{Q}(\tau)$ describing

the efficacy of a particular ramp process. We then discuss the scaling of such a function with respect to the ramp's duration τ.

Hereafter we will employ numerical methods, including common ODE tools and the methods outlined in Chapter 3, to analyse the behaviour of these ramps in the context of both the variational equations in section 4.3 and the GPE in section 4.4.

Section 4.3 will pertain to numerical solutions of the Thomas-Fermi and Gaussian variational equations. We will confirm numerically the scaling arguments made earlier in the chapter regarding the τ dependence of the function $\mathcal{Q}$. We find that $\mathcal{Q}(\tau)$ has a predictable power law decay, and also oscillates with some frequency Ω. We find that this frequency tracks closely behind the natural breathing frequency of the condensate system at the end of the ramp, ie. $\Omega \approx \omega_B(U_f)$

In section 4.4 we repeat the analysis discussed above for the GPE. As the quantities we are sampling are of an order $\sim 10^{-10}$ at times, the propagation of errors due to subtracting two very small numbers necessitates a very high precision in our evolution and sampling. For this reason, we will analyse in detail the propagation of errors in, and convergence of, our numerical calculations. We will then compare this GPE data to the variational equivalents, paying attention to the respective power law exponents and frequencies as in the variational case.

4.2 Inverse engineered shortcuts to adiabaticity

The first step in implementing the inverse engineering method to determine shortcuts to adiabaticity is defining the desired trajectory of some system

parameter. In our case this parameter will be the width σ of the BEC cloud. We then use this trajectory as a constraint to compute the corresponding trajectory of our control parameter. In our case, we choose the path of $\sigma(t)$ in the Gaussian variational equation that would yield a ground state to ground state transition, then work backwards to the path of $U(t)$ that generates this.

4.2.1 Target trajectory of $\sigma(t)$ and the polynomial ansatz.

In Chapter 2 we showed that a system obeying the GPE has breathing and quadrupole normal modes which can be approximated using any of the variational equations (2.35), (2.37), or (2.49). For the purposes of this section we assume the dynamics to be described by the single parameter isotropic case of the Gaussian system of equations:

$$\sigma\ddot{\sigma} + \sigma^2 - \sigma^{-2} = \frac{U(t)}{\left(\sqrt{2\pi}\sigma\right)^D}. \tag{4.1}$$

Since this equation is non-linear for $D \neq 2$ we define the function $h(U)$ as a stationary solution to the variational equation above. In general, the target trajectory of the parameter σ is

$$\begin{aligned} R_0(\tilde{t}) &= h(U_i) + \left(h(U_f) - h(U_i)\right)\xi(\tilde{t}) \\ \xi(\tilde{t}) &= \sum_n^N a_n \tilde{t}^n, \quad a_n \in \mathbb{R}, \tilde{t} \in [0,1]. \end{aligned} \tag{4.2}$$

The equation $R_0(\tilde{t})$ and the polynomial $\xi(\tilde{t})$ are parametrised by the length of the ramp τ where each of these ramps are defined on the interval $\tilde{t} \in [0,1]$ and $\tilde{t} = \frac{t}{\tau}$. The choice of polynomial ξ and the function $h(U)$ determines the specific trajectory $U(\tilde{t})$ we find. In order to determine a suitable solution for

ξ we impose the boundary conditions on equation (4.2)

$$R_0(0) = h(U_i), \quad R_0(1) = f(U_f),$$
$$\dot{R}_0(0) = \dot{R}_0(1) = \ddot{R}_0(0) = \ddot{R}_0(1) = 0. \tag{4.3}$$

Conditions at the beginning of the ramp ie. at $t = 0$ imply the system begins in its ground state as $R_0(0) = \sigma_0$. Similarly the conditions at the end of the ramp ie. at $t = \tau$ imply the system ends the process in its ground state also. Together these conditions, if fulfilled, ensure a ground state to ground state transition with no induced excitations. These conditions then imply the corresponding conditions on the ramp polynomial $\xi(1) = 1$, $\xi(0) = \dot{\xi}(0) = \dot{\xi}(1) = \ddot{\xi}(0) = \ddot{\xi}(1) = 0$. Imposing these conditions on the general N^{th} order polynomial $\xi(\tilde{t})$ leads to the system of equations

$$\sum_n^N a_n = 1 \qquad \sum_n^N n a_n = 0 \quad , \quad \sum_n^N (n-1)\, n a_n = 0. \tag{4.4}$$

From here we must make a choice regarding the solution to (4.4) as well as the function $h(U)$ approximating the stationary width of the condensate in relation to U. Over the remainder of section 4.2 we outline a number of these choices and their resulting interaction ramps.

4.2.2 Ramps in the Thomas-Fermi limit

By ignoring the contributions of the σ^{-2} term in equation (4.1) we find the approximate solution $h(U) = \left(U/\sqrt{2\pi}\right)^{\frac{1}{2+D}}$. For simplicity for this section we assume the system is one dimensional so $h(U) = \left(U/\sqrt{2\pi}\right)^{\frac{1}{3}}$. This approximation to the isotropic equation of motion along with taking the lowest order solution to the system of equations determining $\xi(\tilde{t})$ at $N = 5$ leads to the polynomial $\xi(\tilde{t}) = 10\tilde{t}^3 - 15\tilde{t}^4 + 6\tilde{t}^5$. After inserting the target

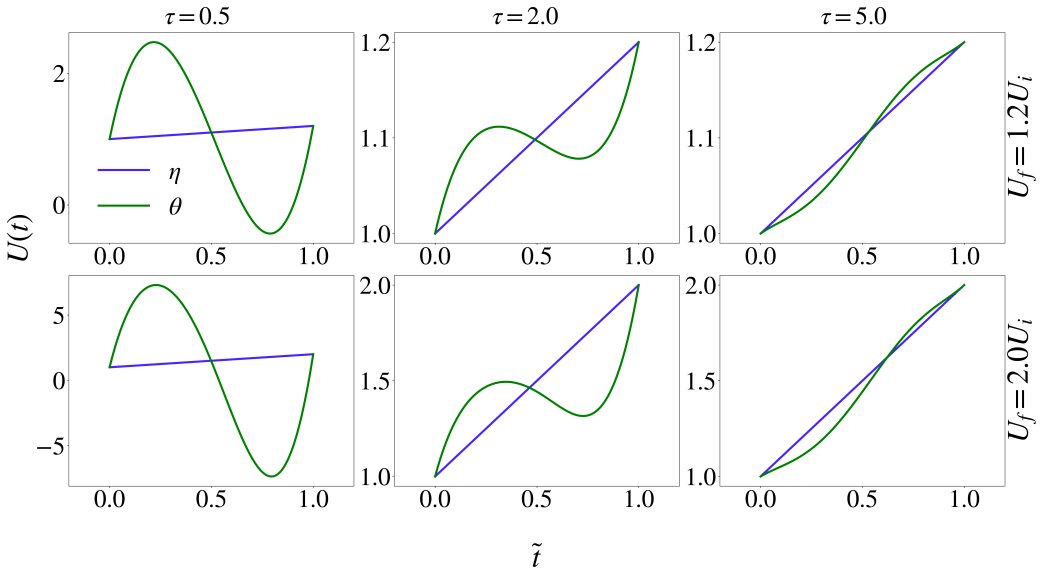

Figure 4.1: Ramp trajectories in the Thomas-Fermi limit for $N = 5$ polynomial ramp $\theta(\tilde{t})$ equation (4.5) and linear $\eta(\tilde{t})$ ramp, $\tau = \{0.5, 2.0, 5.0\}$, $U_i = 1.0$.

path $R_0(\tilde{t})$ into the isotropic equation of motion we find the ramp trajectory $U(\tilde{t}) = \theta(\tilde{t})$:

$$\theta(\tilde{t}) = \left(U_i^{1/3} + \lambda\xi(\tilde{t})\right)^2 \times \left(U_i^{1/3} + \lambda\ddot{\xi}(\tilde{t}) + \lambda\xi(\tilde{t})\right), \quad \lambda = U_f^{1/3} - U_i^{1/3}. \quad (4.5)$$

For ease of notation, we also define a linear interaction ramp as $\eta(\tilde{t})$. A number of the curves generated by this function, as well as the $\eta(\tilde{t})$ linear ramp, are shown in figure 4.1. We can see from figure 4.1 that when the duration of the ramp τ is below some threshold, $\theta(\tilde{t})$ temporarily causes the system to obtain negative (attractive) interactions. In this case the ground state of the system would become qualitatively different from the Gaussian ansatz we have chosen and this variational approximation would likely break down. For this reason we largely ignore these shortest duration ramps in the analysis to follow.

4.2.3 Efficiency metric for interaction ramps

The goal of these interaction ramps is to vary the parameter U from some initial value U_i to some final value U_f whilst avoiding unwanted excitations in the final target state. We begin at $t = 0$ in the ground state ψ_0 at $U = U_i$. In the case of a perfectly adiabatic transition, the wavefunction after this evolution from $t = 0$ to $t = \tau$ will be the ground state in the new system at $U = U_f$. In the case of a trajectory resulting in a less than perfect replication of the final system's ground state we require a metric by which to measure how well each trajectory has performed. In many of the applications discussed in Chapter 1, the energy added to the system is often of primary concern. For that reason, we use a metric based on the deviation from the ground state energy at the current interaction strength $U = U(t)$ and time t to determine the effectiveness of our scheme,

$$\mathcal{Q}(t) = E[\psi_t] - E_0^t. \tag{4.6}$$

, where E_0^t is the ground state energy of the system at time t and $U = U(t)$.

4.2.4 Approximate scaling of excess energy

As the derivation of the $\theta(\tilde{t})$ ramp assumes a Thomas-Fermi like solution to the isotropic equation, we do not expect to see a true shortcut to adiabaticity. As θ is a smooth continuous function however we would expect it to eventually approach adiabaticity at large timescales τ. We might then try to understand how the excess energy function $\mathcal{Q}(\tau)$ behaves in the intermediate regions between $\tau = 0$ instantaneous ramps and $\tau \to \infty$ adiabatic ramps. For this we define a function of the parametrised time coordinate $\tilde{t}$

$$f(\tilde{t}) = \sigma(\tilde{t}) - R_0(\tilde{t}) \tag{4.7}$$

, describing the deviation of σ from the target radius path. The excess energy $\mathcal{Q}$ should then scale as the square of this deviation when evaluated at the endpoint of the ramp $\tilde{t} = 1$. The true behaviour of $f(\tilde{t})$ is likely intractibly complicated as we cannot solve for $\sigma(\tilde{t})$ directly. However, we can consider a simplified scenario in which the small radius oscillations along the ramp trajectory are ignored and the fluctuations at $\tilde{t} = 1$ come purely from the derivative of $f(\tilde{t})$ as

$$f(t < \tau) = 0 \quad , \quad f'(t < \tau) \neq 0. \tag{4.8}$$

For reference, the target radius paths of the linear and manufactured ramps $R_0^\eta(\tilde{t})$ and $R_0^\theta(\tilde{t})$ respectively are

$$R_0^\eta(\tilde{t}) = h(U_i) + (h(U_f) - h(U_i))\,\tilde{t}, \tag{4.9}$$

$$R_0^\theta(\tilde{t}) = \left(\frac{U_i}{\sqrt{2\pi}}\right)^{1/3} + \left(\left(\frac{U_f}{\sqrt{2\pi}}\right)^{1/3} - \left(\frac{U_i}{\sqrt{2\pi}}\right)^{1/3}\right)\xi(\tilde{t}). \tag{4.10}$$

To understand the scaling of $f'(\tilde{t})$ then we need to compute or approximate that of $\sigma'(\tilde{t})\Big|_{\tilde{t}=1}$ and $R_0'(\tilde{t})\Big|_{\tilde{t}=1}$. Intuitively it seems $\sigma'(\tau)$ should have an oscillatory mode plus some overall decay. In figure 4.2 we check this assumption numerically for a number of ramps. From here we see $\sigma' \sim \tau^{-1}$ and $\sigma' \sim \tau^{-3}$ for the linear and manufactured ramps respectively. Define these exponents as α^η and α^θ. The scaling of the function $f^{i\prime}$ for $i = \{\eta, \theta\}$ then is

$$f^{i\prime}(\tilde{t}) \sim R_0^{i\,\prime}(\tilde{t}) + \tau^{-\alpha^i}. \tag{4.11}$$

By differentiating equations (4.9) and (4.10) we find the target paths R_0^i scale identically to σ' for both the linear and manufactured ramps. It follows then that $f^{i\prime}(\tilde{t}) \sim \tau^{-\alpha^i}$. Now assume $f(t' = t > \tau)$ is of the form

$$f(t') = \rho \sin(\Omega t') \Rightarrow f'(t') = -\Omega\rho\cos(\Omega t'). \tag{4.12}$$

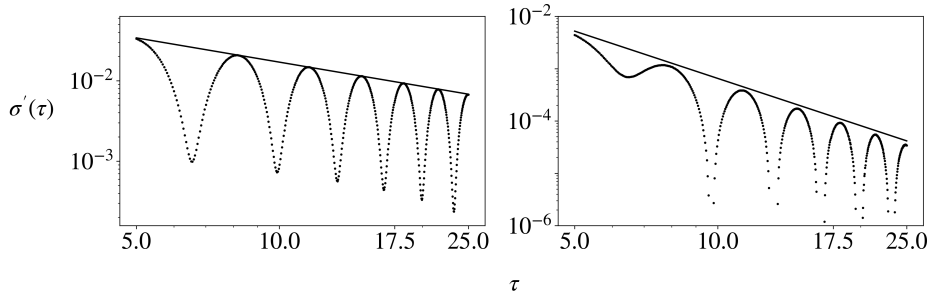

Figure 4.2: Scaling of $\sigma'(\tau)$ for ramps over $\tau = \{5, ..., 25\}$. (left) Linear ramp, solid line is a τ^{-1} decay. (right) Manufactured ramp, solid line is a τ^{-3} decay.

Evaluating this at $t = \tau$ or $t' = 0$ and equating the result to $f'(\tilde{t})$ leads to the scaling of $f'(\tau)$

$$\begin{aligned} f^{i\prime}(\tau) &= -\Omega\rho = c\tau^{-\alpha^i} \\ \Rightarrow \rho^i \sim \tau^{-\alpha^i} &\Rightarrow f^i(t > \tau) \sim \tau^{-\alpha^i} \Rightarrow \mathcal{Q}^i(\tau) \sim \tau^{-2\alpha^i}. \end{aligned} \tag{4.13}$$

For linear ramps then we have $\mathcal{Q}^\eta(\tau) \sim \tau^{-2}$ and manufactured ramps $\mathcal{Q}^\theta(\tau) \sim \tau^{-6}$.

These results offer no more than an approximate qualitative description of the overall $\mathcal{Q}(\tau)$ response to various ramp shapes and durations. In the following section we will perform a numerical analysis of the linear $\eta(\tilde{t})$ and manufactured $\theta(\tilde{t})$ ramp shapes to determine their effectiveness in both the variational regime as well as for the full GPE model. Before we move on however, we note an alternative ramp shape that meets the requirements of equation 4.4 whilst providing an exact shortcut to adiabaticity at any τ.

4.2.5 An exact shortcut to adiabaticity in two dimensional systems

When considered in two dimensions, the Gaussian isotropic variational equation becomes solvable. This allows for the exact solution σ_0 to the stationary equation

$$\sigma_0 = \left(\frac{U}{2\pi} + 1\right)^{1/4}. \tag{4.14}$$

By following the procedure as outlined in subsections 4.2.2 and 4.2.1, this solution leads to the interaction ramp

$$\kappa(\tilde{t}) = 2\pi\left\{\left(\lambda_1\left(\xi(\tilde{t}) + \ddot{\xi}(\tilde{t})\right) + \lambda_0\right) \times \left(\lambda_0 + \lambda_1\xi(\tilde{t})\right)^3 - 1\right\}. \tag{4.15}$$

Here λ_0 and λ_1 are defined as

$$\lambda_0 = \left(\frac{U_i}{2\pi} + 1\right)^{1/4}, \tag{4.16}$$

$$\lambda_1 = \left(\frac{U_f}{2\pi} + 1\right)^{1/4} - \left(\frac{U_i}{2\pi} + 1\right)^{1/4}. \tag{4.17}$$

We will see in figure 4.8 (c) that this ramp yields zero excess energy when implemented in a system with dynamics obeying the two dimensional Gaussian variational equation.

4.3 Performance of engineered ramps - Variational equations

In this section, we will use numerical simulations of the variational equations to analyse the effect of the interaction ramps discussed in the previous section on the excess energy $\mathcal{Q}(\tau)$. Unless mentioned otherwise, we will only be considering comparisons between the fifth order manufactured ramp $\theta(\tilde{t})$

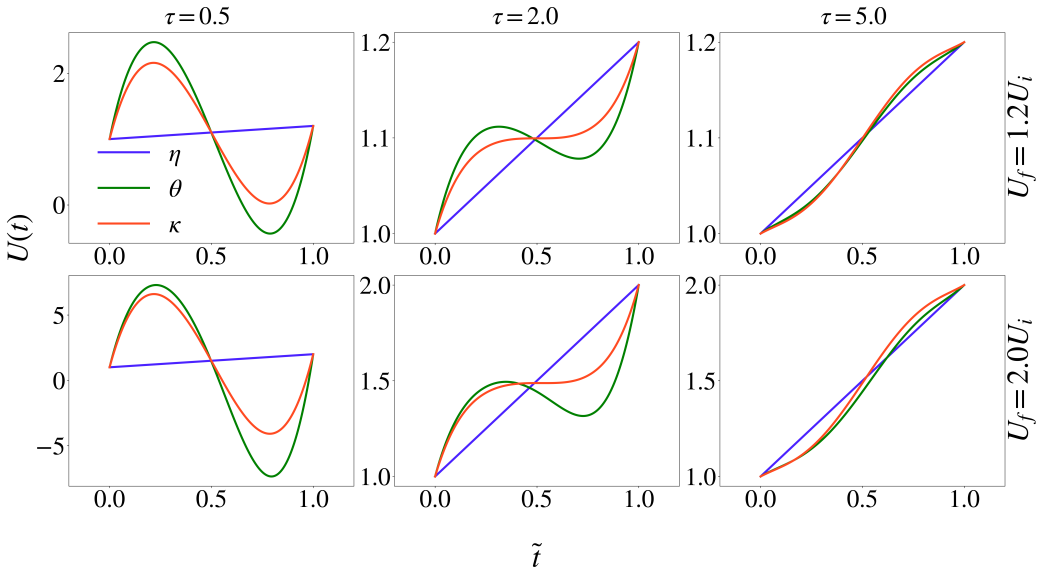

Figure 4.3: Ramp trajectories: exact $\kappa(\tilde{t})$, Thomas-Fermi $\theta(\tilde{t})$ and linear $\eta(\tilde{t})$ ramps using the two dimensional variational equation (4.15), $\tau = \{0.5, 2.0, 5.0\}$, $U_i = 1.0$ and $U_f = 1.2U_i$ and $2.0U_i$.

equation (4.5) and linear $\eta(\tilde{t})$ ramps. Numerical data will come from the isotropic Gaussian variational equation mainly in one dimension, but we will also show a two-dimensional calculation in figure 4.8.

4.3.1 Time dependence of radius and excess energy

Before analysing the excess energy at the end of a ramp $t = \tau$ we would like to first understand how the radius $\sigma(\tilde{t})$ and excess energy $\mathcal{Q}(\tilde{t})$ of a wavefunction reacts in the intermediate times $0 < t < \tau$ under the action of $\theta(\tilde{t})$ and $\eta(\tilde{t})$ ramps. As we derived the $\theta(\tilde{t})$ ramp under a Thomas-Fermi approximation, we would expect to see a significantly more efficient ramp when the average interaction strength of the ramp is large.

In figure 4.4 we show the radius dynamics, ramp path and excess energy for ramps in this small τ region. What is evident from this initial data is a clear

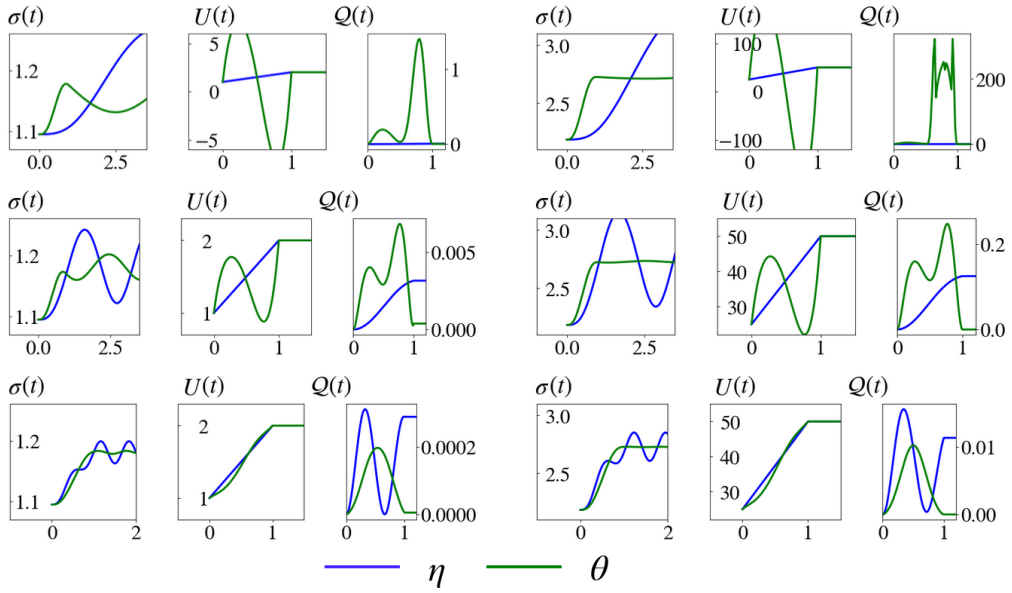

Figure 4.4: Radius dynamics $\sigma(t)$ equation (2.37) over manufactured $\theta(\tilde{t})$ ramp equation (4.5) and linear $\eta(\tilde{t})$ ramp. Excess energy $Q(t) = E_t - E_0[U(t)]$, parameters (left) $(U_i, U_f) = (1, 2)$ (right) $(U_i, U_f) = (25, 50)$, $\tau = \{0.5, 1.5, 5.0\}$ for each row respectively.

decay in the amplitude of radius dynamics at the end of the $\theta(\tilde{t})$ ramp when U is large as we expected. Excess energy measurements are likely decaying in tandem but are not clearly visible from this data.

Conversely, the linear $\eta(\tilde{t})$ ramps have the opposite effect, producing larger amplitude radius oscillations as well as larger excess energy at larger mean values of the interaction strength.

4.3.2 Dependence of excess energy on ramp duration

Regarding the excess energy remaining at the end of a ramp, there are a number of features we can examine. For example, the mean value of a $\mathcal{Q}(\tau)$ curve with respect to the average interaction strength shows a decay for the

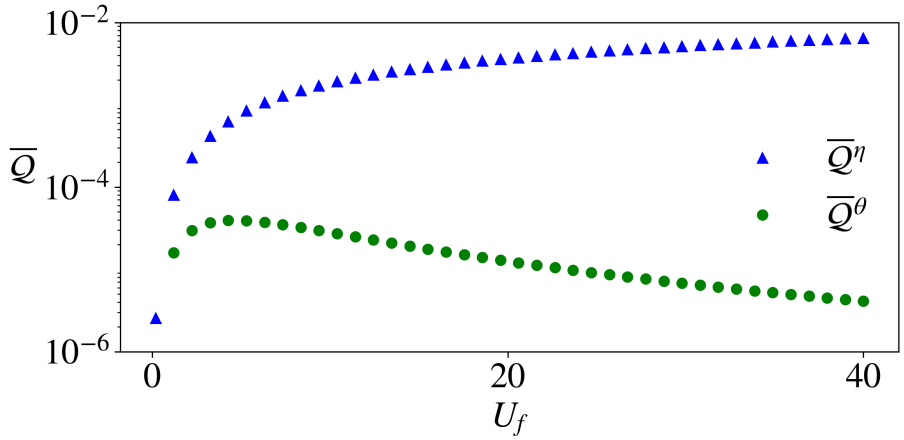

Figure 4.5: Mean excess energies $\bar{\mathcal{Q}}$ (averaged over τ) versus U_f with $U_f = 2U_i$ and $\tau = \{1, ..., 40\}$.

manufactured θ ramp and a growth for the η linear ramp. This behaviour can be justified by noting the Thomas-Fermi like approximation used in the derivation of the manufactured ramp leads to a more effective ramp process with lesser excess energy at large values of U. The two quantities we focus on here however will be the power law scaling of $\mathcal{Q}$ with τ, namely the parameter ν in $\tau^{-\nu}$, and the frequency of oscillation Ω of $\mathcal{Q}(\tau)$.

In figure 4.7 we plot the $\nu = 2$ and $\nu = 6$ values approximated earlier in this chapter against the numerical $\mathcal{Q}(\tau)$ data for a number of values of (U_i, U_f). In the instance tested these curves approximate an upper envelope of the numerical data. To estimate the frequency of this $\mathcal{Q}(\tau)$ data, and for a more thorough confirmation of this decay rate, it is helpful to have a model function. We find that a shifted and rescaled cosine function of the form $g(\tau) = a\tau^{-2} + b\tau^{-2}\cos(c + \Omega\tau)$ is fit for this purpose excluding small $\tau \sim 1$ ramps. An example of this model and a least squares estimation of its parameters is shown in figure 4.7. Using this model we can sample the frequency of oscillation Ω and a larger number of decay exponents ν. We

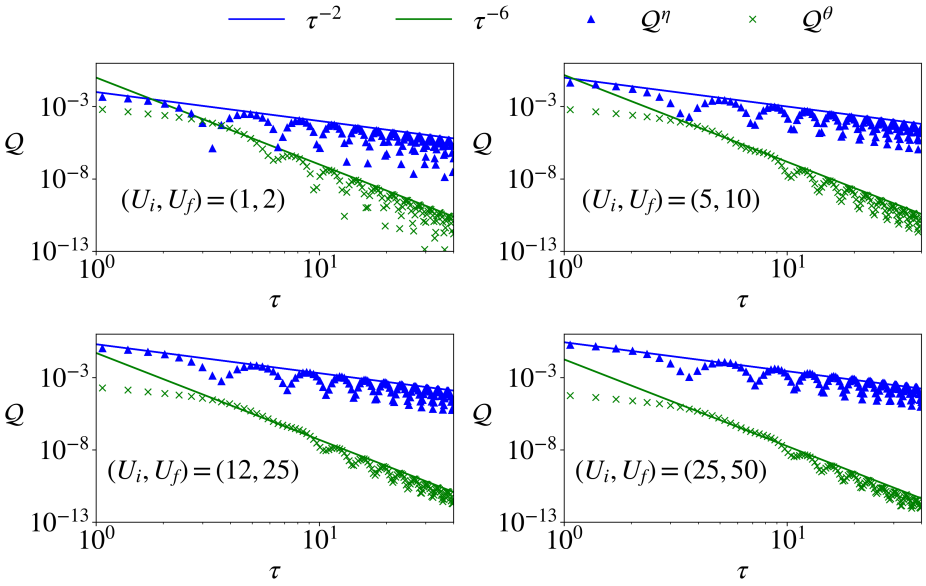

Figure 4.6: Excess energies from the isotropic Gaussian equation for ramps with $U_f/U_i = 2$.

find the decay exponents are constant with respect to the average interaction strength. We also see that the excess energy frequency Ω closely follows the breathing frequency of the condensate at $U = U_f$. A number of fits with the decay exponents $\nu = 2$ and $\nu = 6$ are shown in figure 4.7. The $\Omega(U_f)$ frequency data is shown in figure 4.8 along with the breathing mode frequency at $U = U_f$.

To summarise this data we have provided excess energy data for a grid of U_i and τ parameters also in figure 4.8 **(a)**.

We also show excess energy data for the two-dimensional ramp variant $\kappa(\tilde{t})$ equation 4.15 and the previous manufactured ramp $\theta(\tilde{t})$ both calculated in two dimensions in figure 4.8 **(c)**. Note the $\theta(\tilde{t})$ excess energy data in two dimensions lacks the frequency variation we see in the one dimensional implementations due to the constant breathing frequency of two-dimensional systems. When considered alongside the discussion which we will present in

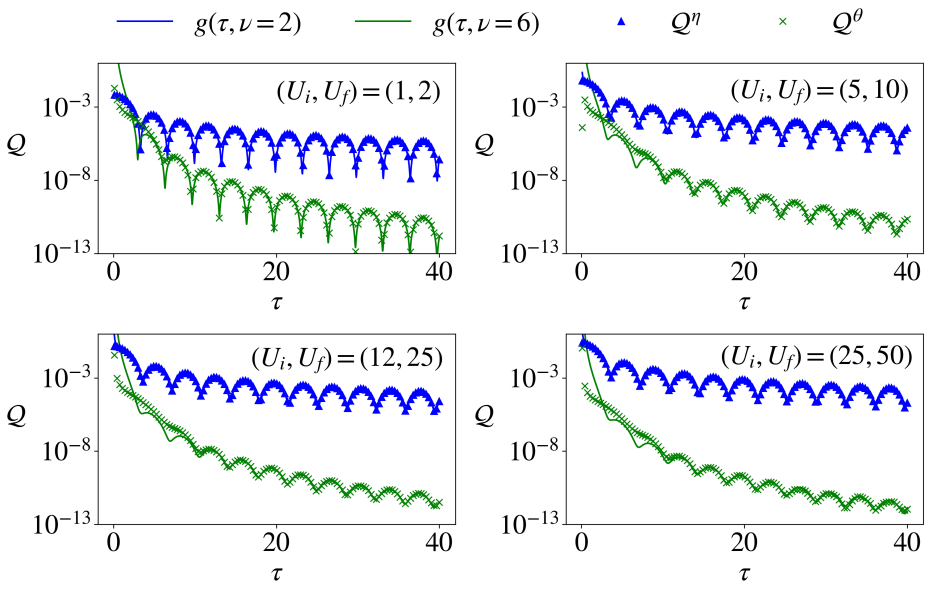

Figure 4.7: Model $g(\tau) = \tau^{-\nu}(a + b\cos(c + \Omega\tau))$ fit to $\mathcal{Q}(\tau)$ data for linear $\eta(\tilde{t})$ with $\nu = 2$ and fifth order manufactured $\theta(\tilde{t})$ ramp with $\nu = 6$.

subsection 4.4.2, this data further builds on the connection between natural breathing frequencies ω and the frequencies of the excess energy curves Ω.

4.4 Performance of engineered ramps - GPE

In this section, we repeat the excess energy analysis of the previous section whilst using the GPE for our simulations rather than the variational equations. As this involves the evolution of a PDE rather than an ODE, the discretisation of space and time are of much greater importance. For this reason, we take some time initially to understand the effect of discretisation on our calculations of $\mathcal{Q}(\tau)$ curves. We collect three distinct sets of $\mathcal{Q}(\tau)$ data for a particular choice of (U_i, U_f): one control set with discretisation (dx_1, dt_1), one with a fine spatial mesh (dx_2, dt_1), and one with a fine time mesh (dx_1, dt_2). We then vary the step size parameter pairs dx and dt until

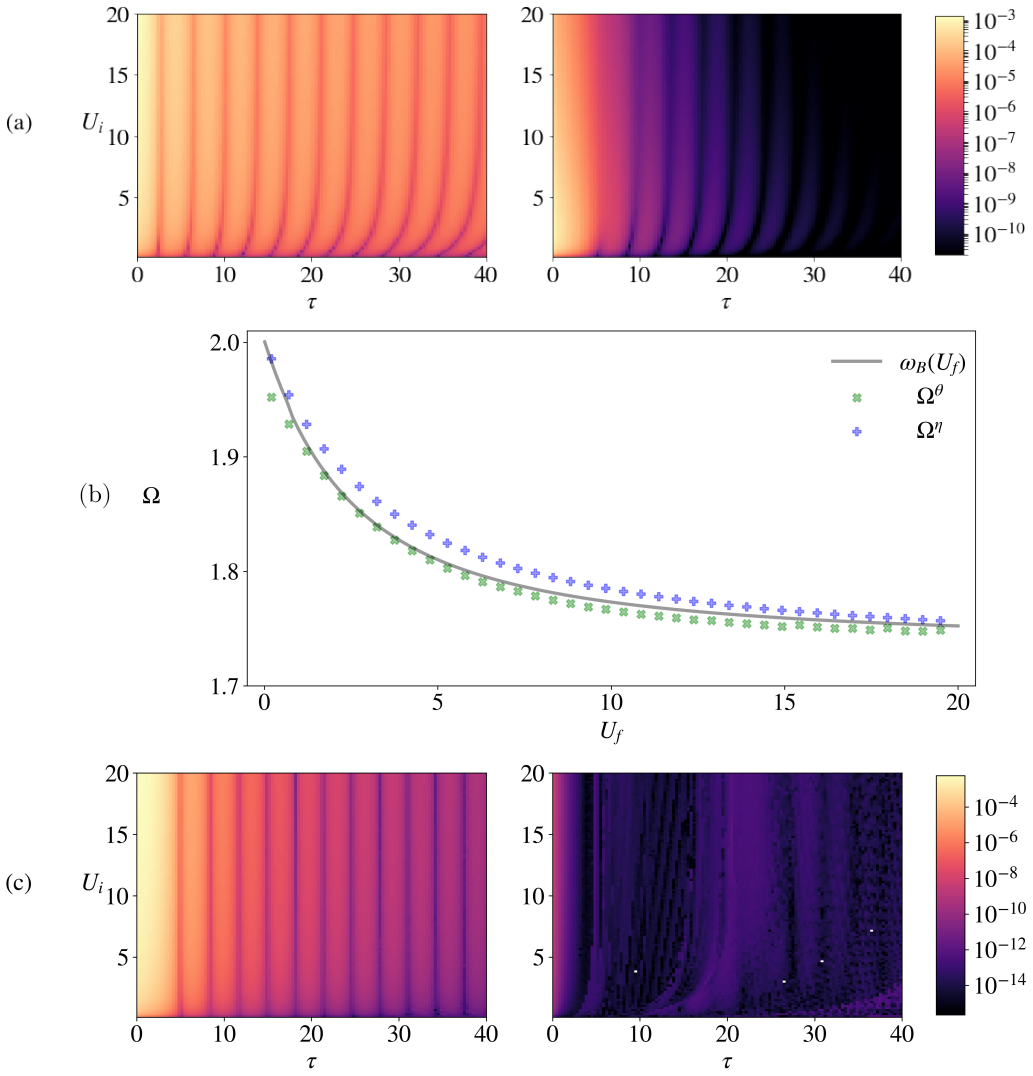

Figure 4.8: Ramp excess energy comparisons using gaussian isotropic equation. **(a)** Excess energy data for (left) linear $\eta(\tilde{t})$ and (right) manufactured $\theta(\tilde{t})$ ramps in one dimension with $U_i = \{1, ..., 20\}$, $U_f = 2U_i$, and $\tau = \{1, ..., 40\}$. **(b)** Frequencies Ω of $\mathcal{Q}$ versus U_f for linear η and manufactured θ ramp. Also shown are the breathing frequencies ω_B at $U = U_f$. **(c)** (left) Manufactured $\theta(\tilde{t})$ showing constant frequency $\mathcal{Q}(\tau)$ due to constant breathing frequency in two dimensions. (right) Zero excess energy (to machine precision) using exact shortcut ramp $\kappa(\tilde{t})$ in two dimensions.

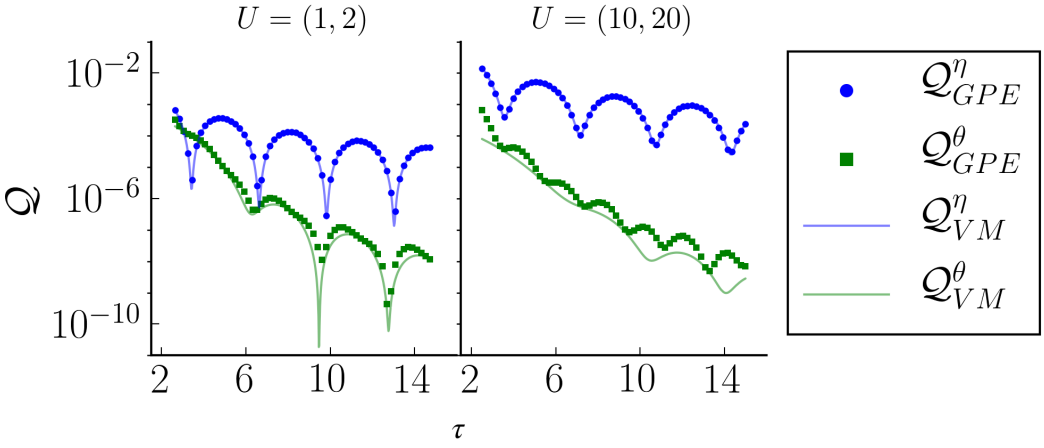

Figure 4.9: Comparison of variational equation excess energy data to that of the GPE. Parameters for imaginary time evolution step update criteria: $\delta = 100, \epsilon = 10^{-14}$, $n = (20'000, 100'000)$ for left and right figures respectively, discretisation: $dx = 0.00025$, $dt = 0.001$.

these data sets are consistently converged to at least 2 orders of magnitude less than the smallest $\mathcal{Q}(\tau)$ data point.

In figure 4.9 we use these converged discretisation parameters to compare our variational data to that of the GPE. As we would expect, the two methods tend to diverge somewhat as we increase the average interaction strength of the system.

4.4.1 Dependence of excess energy on ramp duration

In the GPE data, we find more deviations from the $g(\tau)$ model used in section 4.3, particularly at low $\mathcal{Q}$ values due to numerical precision issues. We also of course cannot collect as much data as we could with the variational equations. However we can still make some sparse measurements for the quantities Ω and ν. In figure 4.10 we show the $g(\tau)$ model from the previous section

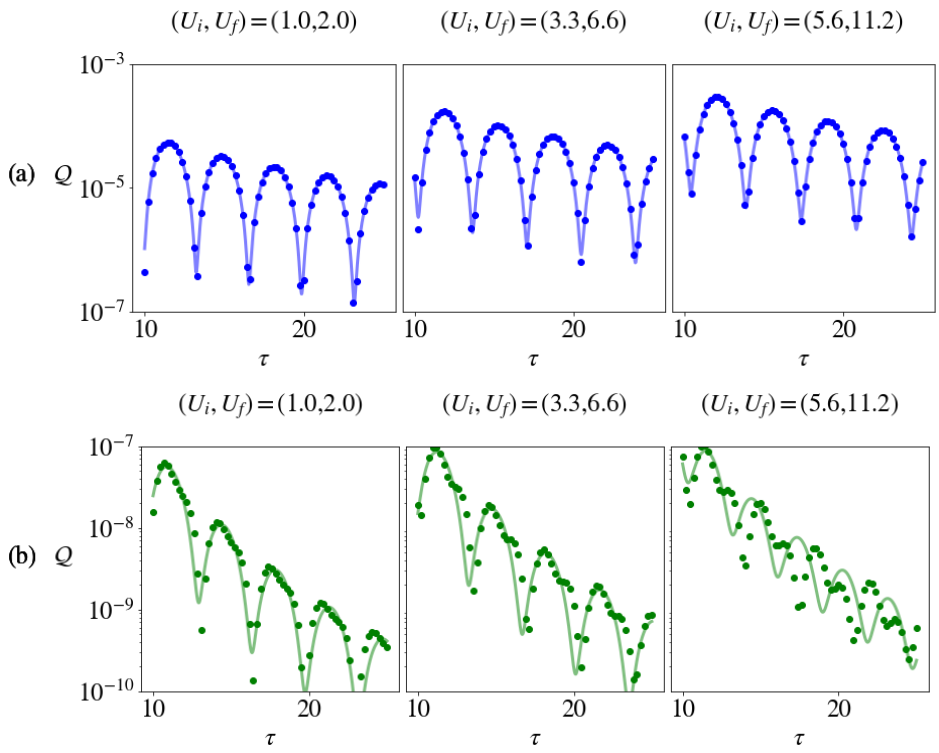

Figure 4.10: $g(\tau) = \tau^{-\nu}(a + b\cos(c + \Omega\tau))$ model fit to **(a)** linear $\eta(\tilde{t})$ ramp data and **(b)** $\theta(\tilde{t})$ manufactured ramp data. Parameters and discretisation used: $\delta = 100$, $\epsilon = 10^{-14}$, $n = 50'000$, $dx = 0.00025$, $dt = 0.001$.

fitted to GPE $\mathcal{Q}$ data for ramps of $(U_i, U_f) = \{(1, 2), (3.0, 6.6), (5.6, 11.2)\}$ for both linear $\eta(\tilde{t})$ and fifth order manufactured $\theta(\tilde{t})$ ramps. We note that although this $g(\tau)$ model reproduces the characteristics of the linear η ramps reasonably well, it fails to reproduce the behaviour of the θ ramps, particularly at large U. We find it is necessary to include a second and third oscillatory term to approximate the data accurately. An example of such a fit for a model of the form $f(\tau) = \tau^{-6}(a + b\cos(c + \omega_1\tau) + d\cos(e + \omega_2\tau) + f\cos(g + \omega_g\tau))$ is provided in figure 4.11. The first two frequencies can be approximately identified as the breathing frequency ω_B and twice the breathing frequency $2\omega_B$. The third frequency is not identified with any

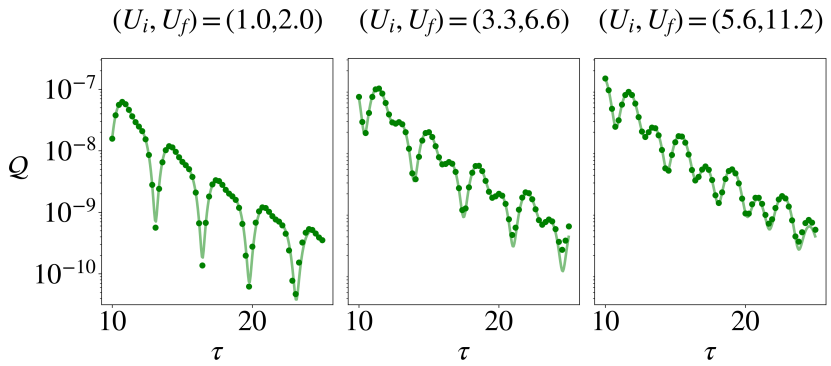

Figure 4.11: $f(\tau) = \tau^{-6}(a + b\cos(c + \omega_1\tau) + d\cos(e + \omega_2\tau) + f\cos(g + \omega_g\tau))$ model fit to $\theta(\tilde{t})$ manufactured ramp data. Parameters and discretisation used: $\delta = 100$, $\epsilon = 10^{-14}$, $n = 50'000$, $dx = 0.00025$, $dt = 0.001$.

particular dynamical mode, but it is necessary to achieve an appropriate fit to the data. Fitting this model to a number of $\mathcal{Q}(\tau)$ curves we find the first frequency ω_1 matches the data from the variational equation provided in figure 4.8 **(b)**. All three frequencies of the $f(\tau)$ model data shown in figure 4.11 are shown in table 4.1. Note the third frequency is not always present in any significant quantity in the fitted parameters but is still necessary to achieve a proper fit to the data.

4.4.2 Physical reasoning for breathing frequency dependence of $\mathcal{Q}(\tau)$

The appearance of the ω_B breathing frequancy quantity in the $\mathcal{Q}(\tau)$ data can be interpreted most intuitively in the context of the Gaussian variational equation. If we consider an instance of the $\theta(\tilde{t})$ manufactured ramp from U_i to U_f the radius of the cloud would vary as $\sigma(\tilde{t})$. Although the system would begin at $\tilde{t} = 0$ in its ground state σ_0, once U begins to vary, σ will again begin to oscillate with some frequency. When these oscillations line

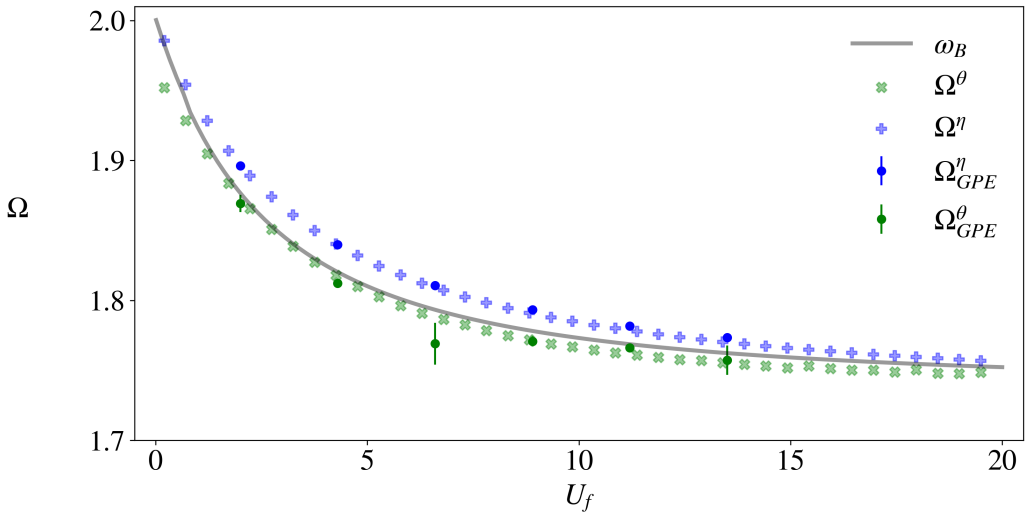

Figure 4.12: First frequency ω_1 from the model shown in figure 4.11 for GPE $\mathcal{Q}(\tau)$ data.

up with the length of a ramp, ie. a point with $\sigma'(\tau) = 0$ (where the $'$ represents differentiation with respect to $\tilde{t}$), the radius of the cloud $\sigma(\tau)$ adopts the ground state of the new system. The frequency in τ of these exact shortcuts would be expected to fall in the region between the natural breathing frequency at the initial $U = U_i$ value, and the final $U = U_f$ value. We see from the data shown in figures 4.8 and 4.12 that this frequency closely follows the breathing frequency at the final U value $\omega_B(U_f)$.

ω	$U = (1, 2)$	$U = (3.3, 6.6)$	$U = (5.6, 11.2)$
fitted parameters			
ω_1	1.869 ± 0.006	1.78 ± 0.01	1.764 ± 0.001
ω_2	3.75 ± 0.05	3.54 ± 0.04	3.427 ± 0.001
ω_3	0.0006 ± 0.0007	$2 \times 10^{-5} \pm 6 \times 10^{-5}$	0.21 ± 0.02
breathing mode			
$\omega_B(U_f)$	1.87474...	1.78977...	1.76513...

Table 4.1: Frequency parameters returned from a least squares optimisation of the model $f(\tau)$. First two frequencies are approximately $(\omega_1, \omega_2) \approx (\omega_B, 2\omega_B)$.

Chapter 5

Summary and outlook

In this thesis we have studied dynamical modes of Bose Einstein condensates as well as shortcuts to adiabaticity for ramps in the interaction strength of such a system. In this chapter we will summarise the results and findings of previous chapters, the limitations of said analysis, and suggest avenues for further research.

5.1 Discussion

In Chapter 2 a variational analysis for the dynamical modes of a Bose Einstein condensate is carried out. By these methods the dynamics of a cloud of weakly interacting Bosons are approximated using the mean field Gross-Pitaevskii equation. This mean field description is then further simplified as various systems of nonlinear ordinary differential equations. By this analysis, we reproduce some existing results regarding the characteristic frequencies of normal modes. In particular we characterise the breathing and quadrupole dynamical modes in terms of their frequencies. We also reproduce an analysis

of resonant like behaviour appearing in similar systems with a modulated interaction strength [11, 58].

Chapter 3 mainly focused on the numerical methods used for solving the Gross-Pitaevskii equation. We discuss the symplectic integration schemes and imaginary time algorithms which are used in the remainder of the analysis. We then implement these techniques for solutions of the Gross-Pitaevskii equation in one dimension. We largely focus on understanding the degree to which our variational calculations approximate Gross-Pitaevskii dynamics.

In Chapter 4 we determine a shortcut protocol for ramps in the interaction strength U. We then investigate some features of this shortcut ramp's function in the context of the Gaussian variational equation and the Gross-Pitaevskii equation. Shortcuts to adiabaticity in Bose-Einstein condensates have appeared in the literature in a number of contexts [30, 34, 36–39] using various methods. We have continued the analysis of the excess energy generated by shortcut processes derived using the methods of inverse engineering. The magnitude of excess energy curves are found to decay as a power law relationship of the form $\tau^{-\nu}$. In the case of our Thomas-Fermi manufactured ramp we find a $\nu = 6$ decay, an improvement over the $\nu = 2$ linear process. We have demonstrated that this power law relationship lingers beyond the variational approximations we have made to appear in full Gross-Pitaevskii calculations also.

The frequency with which the induced excitations oscillate in τ has also been studied in the context of variational methods as well as the Gross-Pitaevskii equation. We see that these excitation frequencies can be closely approximated by the characteristic frequency of the breathing mode in the final $U = U_f$ system. We see the Gaussian variational equation offers an excellent approximation of these induced excitations when compared to the

Gross-Pitaevskii equation. This oscillatory behaviour has been interpreted in some studies, particularly in [74], as an *accidental shortcut* when the duration of a particular ramp process coincides with the wavelength of radius oscillations in the condensate. In linear ramp processes these accidental shortcuts tend to approach exact shortcut processes ie. generate zero excess energy. In our polynomial ramp processes, the excess energy curves tend to decay significantly faster as a whole but do not approach zero at their minima. Rather they oscillate about a finite value in line with a τ^{-6} decay. In Gross-Pitaevskii calculations, we find the induced excitations oscillate with three distinct frequencies. The breathing mode continues to be the dominant frequency, followed by its first harmonic, and a third frequency currently unidentified with any physical quantity.

5.2 Future research questions

Several avenues for additional research present from the current study. An investigation of these processes in Bose Einstein condensates beyond mean field Gross-Pitaevskii methods would certainly be of interest. Exact diagonalisation techniques for example might be applied to systems with a small number of Bosons under the action of these shortcut protocols. We also note that our analysis is limited in some regards as our variational analysis does not allow for all dynamical modes present in the Gross-Pitaevskii system. A further discussion of the induced excitations using a variational equation allowing for dipole and other surface type excitations would be of interest in future studies.

Additionaly we found a symmetry in two-dimensional systems could be lever-

aged to determine an exact shortcut to adiabaticity. Another possible avenue of future research would be to implement this two-dimensional shortcut trajectory in a pseudo one or two-dimensional Bose Einstein condensate by way of the anisotropic variational equations of motion we discussed in Chapter 2 or full three-dimensional Gross-Pitaevskii calculations. The transition between exact shortcut trajectories for two dimensional systems to approximate shortcuts in a pseudo one or two-dimensional cigar or disc shaped condensate may provide interesting insights.

Bibliography

[1] M. Schwartz, "Lectures on Statistical Mechanics: Lecture 12 - Bose-Einstein Condensation," 2019. available at M. Schwartz *harvard.edu* webpage.

[2] M. Anderson, "J. R. Ensher, MR Matthews, CE Wieman, and EA Cornell. Observation of Bose-Einstein condensation in a dilute atomic vapor," *Science*, vol. 269, no. 5221, pp. 198–201, 1995.

[3] E. P. Gross, "Hydrodynamics of a superfluid condensate," *Journal of Mathematical Physics*, vol. 4, no. 2, pp. 195–207, 1963.

[4] L. P. Pitaevskii, "Vortex lines in an imperfect Bose gas," *Sov. Phys. JETP*, vol. 13, no. 2, pp. 451–454, 1961.

[5] J. Rogel-Salazar, "The Gross-Pitaevskii equation and Bose-Einstein condensates," *European Journal of Physics*, vol. 34, no. 2, p. 247, 2013.

[6] N. Karjanto, "The nonlinear Schrödinger equation: A mathematical model with its wide-ranging applications," *arXiv preprint arXiv:1912.10683*.

[7] X. Gao and J. Zeng, "Two-dimensional matter-wave solitons and vortices in competing cubic-quintic nonlinear lattices," *Frontiers of Physics*, vol. 13, no. 1, pp. 1–9, 2018.

[8] B. B. Baizakov, B. A. Malomed, and M. Salerno, "Multidimensional solitons in a low-dimensional periodic potential," *Physical Review A*, vol. 70, no. 5, p. 053613, 2004.

[9] V. G. Ivancevic and D. J. Reid, "Turbulence and shock-waves in crowd dynamics," *Nonlinear Dynamics*, vol. 68, no. 1, pp. 285–304, 2012.

[10] A. L. Fetter and J.-k. Kim, "Vortex precession in a rotating nonaxisymmetric trapped Bose-Einstein condensate," *Journal of low temperature physics*, vol. 125, no. 5, pp. 239–248, 2001.

[11] R. P. Teles, V. S. Bagnato, and F. dos Santos, "Coupling vortex dynamics with collective excitations in Bose-Einstein condensates," *Physical Review A*, vol. 88, no. 5, p. 053613, 2013.

[12] Y. Nikolaieva, A. Olashyn, Y. Kuriatnikov, S. Vilchynskii, and A. Yakimenko, "Stable vortex in Bose-Einstein condensate dark matter," *arXiv preprint arXiv:2103.07856*.

[13] T. Rindler-Daller and P. R. Shapiro, "Angular momentum and vortex formation in Bose-Einstein-condensed cold dark matter haloes," *Monthly Notices of the Royal Astronomical Society*, vol. 422, no. 1, pp. 135–161, 2012.

[14] A. Triay, "Derivation of the dipolar Gross-Pitaevskii energy," *SIAM Journal on Mathematical Analysis*, vol. 50, no. 1, pp. 33–63, 2018.

[15] P. Blakie, C. Ticknor, A. Bradley, A. Martin, M. Davis, and Y. Kawaguchi, "Numerical method for evolving the dipolar projected Gross-Pitaevskii equation," *Physical Review E*, vol. 80, no. 1, p. 016703, 2009.

[16] D. Vudragović and A. Balaž, "Faraday and resonant waves in dipolar cigar-shaped Bose-Einstein condensates," *Symmetry*, vol. 11, no. 9, p. 1090, 2019.

[17] C. Baals, A. G. Moreno, J. Jiang, J. Benary, and H. Ott, "Stability analysis and attractor dynamics of three-dimensional dark solitons with localized dissipation," *Physical Review A*, vol. 103, no. 4, p. 043304, 2021.

[18] R. Flores-Calderón, J. Fujioka, and A. Espinosa-Cerón, "Soliton dynamics of a high-density Bose-Einstein condensate subject to a time varying anharmonic trap," *Chaos, Solitons & Fractals*, vol. 143, p. 110580, 2021.

[19] N. Proukakis, "Beyond Gross-Pitaevskii Mean-Field Theory," in *Emergent Nonlinear Phenomena in Bose-Einstein Condensates*, pp. 353–373, Springer, 2008.

[20] A. Allen, E. Zaremba, C. Barenghi, and N. Proukakis, "Observable vortex properties in finite-temperature Bose gases," *Physical Review A*, vol. 87, no. 1, p. 013630, 2013.

[21] H. Yoshida, "Construction of higher order symplectic integrators," *Physics letters A*, vol. 150, no. 5-7, pp. 262–268, 1990.

[22] G. Strang, "On the construction and comparison of difference schemes," *SIAM journal on numerical analysis*, vol. 5, no. 3, pp. 506–517, 1968.

[23] R. I. McLachlan, "Composition methods in the presence of small parameters," *BIT numerical mathematics*, vol. 35, no. 2, pp. 258–268, 1995.

[24] C. Danieli, B. M. Manda, T. Mithun, and C. Skokos, "Computational efficiency of numerical integration methods for the tangent dynamics of many-body hamiltonian systems in one and two spatial dimensions [j]," *Mathematics in Engineering*, vol. 1, no. 3, pp. 447–488, 2019.

[25] S. Blanes and P. C. Moan, "Practical symplectic partitioned Runge-Kutta and Runge-Kutta-Nyström methods," *Journal of Computational and Applied Mathematics*, vol. 142, no. 2, pp. 313–330, 2002.

[26] W. Bao and Q. Du, "Computing the ground state solution of Bose-Einstein condensates by a normalized gradient flow," *SIAM Journal on Scientific Computing*, vol. 25, no. 5, pp. 1674–1697, 2004.

[27] A. Kordbacheh, S. Szigeti, and A. Martin, "Optical focusing of Bose-Einstein condensates," *arXiv preprint arXiv:2011.14470*.

[28] M. Ma and Z. Huang, "Bright soliton solution of a Gross-Pitaevskii equation," *Applied Mathematics Letters*, vol. 26, no. 7, pp. 718–724, 2013.

[29] M. Born and V. Fock, "Beweis des adiabatensatzes (translation: Proof of the adiabatic theorem," *Zeitschrift für Physik*, vol. 51, no. 3-4, pp. 165–180, 1928. English translation found in "V.A. Fock - Selected Works: Quantum Mechanics and Quantum Field Theory".

[30] A. del Campo, "Shortcuts to adiabaticity by counterdiabatic driving," *Physical review letters*, vol. 111, no. 10, p. 100502, 2013.

[31] E. Torrontegui, S. Martínez-Garaot, A. Ruschhaupt, and J. G. Muga, "Shortcuts to adiabaticity: fast-forward approach," *Physical Review A*, vol. 86, no. 1, p. 013601, 2012.

[32] A. Del Campo, "Frictionless quantum quenches in ultracold gases: A quantum-dynamical microscope," *Physical Review A*, vol. 84, no. 3, p. 031606, 2011.

[33] Q. Zhang, X. Chen, and D. Guéry-Odelin, "Connection between inverse engineering and optimal control in shortcuts to adiabaticity," *Entropy*, vol. 23, no. 1, p. 84, 2021.

[34] X. Chen, A. Ruschhaupt, S. Schmidt, A. del Campo, D. Guéry-Odelin, and J. G. Muga, "Fast optimal frictionless atom cooling in harmonic traps: Shortcut to adiabaticity," *Physical review letters*, vol. 104, no. 6, p. 063002, 2010.

[35] X. Chen, E. Torrontegui, and J. G. Muga, "Lewis-Riesenfeld invariants and transitionless quantum driving," *Physical Review A*, vol. 83, no. 6, p. 062116, 2011.

[36] J.-F. Schaff, X.-L. Song, P. Capuzzi, P. Vignolo, and G. Labeyrie, "Shortcut to adiabaticity for an interacting Bose-Einstein condensate," *EPL (Europhysics Letters)*, vol. 93, no. 2, p. 23001, 2011.

[37] T.-Y. Huang, B. A. Malomed, and X. Chen, "Shortcuts to adiabaticity for an interacting Bose-Einstein condensate via exact solutions of the generalized Ermakov equation," *Chaos: An Interdisciplinary Journal of Nonlinear Science*, vol. 30, no. 5, p. 053131, 2020.

[38] D. Stefanatos, J. Ruths, and J.-S. Li, "Frictionless atom cooling in harmonic traps: A time-optimal approach," *Physical Review A*, vol. 82, no. 6, p. 063422, 2010.

[39] J.-F. Schaff, X.-L. Song, P. Vignolo, and G. Labeyrie, "Fast optimal transition between two equilibrium states," *Physical Review A*, vol. 82, no. 3, p. 033430, 2010.

[40] P. Diao, S. Deng, F. Li, S. Yu, A. Chenu, A. Del Campo, and H. Wu, "Shortcuts to adiabaticity in Fermi gases," *New Journal of Physics*, vol. 20, no. 10, p. 105004, 2018.

[41] D. Papoular and S. Stringari, "Shortcut to adiabaticity for an anisotropic gas containing quantum defects," *Physical review letters*, vol. 115, no. 2, p. 025302, 2015.

[42] D. Guéry-Odelin, J. Muga, M. J. Ruiz-Montero, and E. Trizac, "Non-equilibrium solutions of the boltzmann equation under the action of an external force," *Physical review letters*, vol. 112, no. 18, p. 180602, 2014.

[43] A. Ruschhaupt, X. Chen, D. Alonso, and J. Muga, "Optimally robust shortcuts to population inversion in two-level quantum systems," *New Journal of Physics*, vol. 14, no. 9, p. 093040, 2012.

[44] M. Anderlini, P. J. Lee, B. L. Brown, J. Sebby-Strabley, W. D. Phillips, and J. V. Porto, "Controlled exchange interaction between pairs of neutral atoms in an optical lattice," *Nature*, vol. 448, no. 7152, pp. 452–456, 2007.

[45] S. Fölling, S. Trotzky, P. Cheinet, M. Feld, R. Saers, A. Widera, T. Müller, and I. Bloch, "Direct observation of second-order atom tunnelling," *Nature*.

[46] S. Martínez-Garaot, A. Ruschhaupt, J. Gillet, T. Busch, and J. G. Muga, "Fast quasiadiabatic dynamics," *Physical Review A*, vol. 92, no. 4, p. 043406, 2015.

[47] W. Van Dam, M. Mosca, and U. Vazirani, "How powerful is adiabatic quantum computation?," in *Proceedings 42nd IEEE Symposium on Foundations of Computer Science*, pp. 279–287, IEEE, 2001.

[48] E. Farhi, J. Goldstone, S. Gutmann, and M. Sipser, "Quantum computation by adiabatic evolution,"

[49] T. Keller, T. Fogarty, J. Li, and T. Busch, "Feshbach engine in the Thomas-Fermi regime," *Physical Review Research*, vol. 2, no. 3, p. 033335, 2020.

[50] J. Li, T. Fogarty, S. Campbell, X. Chen, and T. Busch, "An efficient nonlinear Feshbach engine," *New Journal of Physics*, vol. 20, no. 1, p. 015005, 2018.

[51] Y. Ban, X. Chen, E. Torrontegui, E. Solano, and J. Casanova, "Speeding up quantum perceptron via shortcuts to adiabaticity," *Scientific reports*, vol. 11, no. 1, pp. 1–8, 2021.

[52] H. R. Lewis Jr, "Classical and quantum systems with time-dependent harmonic oscillator type Hamiltonians," *Physical Review Letters*, vol. 18, no. 13, p. 510, 1967.

[53] H. R. Lewis Jr and W. Riesenfeld, "An exact quantum theory of the time-dependent harmonic oscillator and of a charged particle in a time-dependent electromagnetic field," *Journal of mathematical physics*, vol. 10, no. 8, pp. 1458–1473, 1969.

[54] J. Guerrero and F. F. López-Ruiz, "On the Lewis-Riesenfeld (Dodonov-Man'ko) invariant method," *Physica Scripta*, vol. 90, no. 7, p. 074046, 2015.

[55] J. M. F. Bassalo, P. d. T. S. Alencar, D. Silva, A. B. Nassar, and M. Cattani, "Ermakov-Lewis Invariants of the Gross-Pitaevskii equation," *arXiv preprint arXiv:0902.3125*.

[56] M. Lohe, "Exact time dependence of solutions to the time-dependent Schrödinger equation," *Journal of Physics A: Mathematical and Theoretical*, vol. 42, no. 3, p. 035307, 2008.

[57] E. Quinn and M. Haque, "Modulated trapping of interacting bosons in one dimension," *Physical Review A*, vol. 90, no. 5, p. 053609, 2014.

[58] I. Vidanović, A. Balaž, H. Al-Jibbouri, and A. Pelster, "Nonlinear Bose-Einstein-condensate dynamics induced by a harmonic modulation of the s-wave scattering length," *Physical Review A*, vol. 84, no. 1, p. 013618, 2011.

[59] Y. Guo, X. Zeng, and H.-S. Zhou, "Energy estimates and symmetry breaking in attractive Bose-Einstein condensates with ring-shaped potentials," in *Annales de l'Institut Henri Poincare (C) Non Linear Analysis*, vol. 33, pp. 809–828, Elsevier, 2016.

[60] Y. Guo and R. Seiringer, "On the mass concentration for Bose-Einstein condensates with attractive interactions," *Letters in Mathematical Physics*, vol. 104, no. 2, pp. 141–156, 2014.

[61] J. Levandosky, "Parabolic and Elliptic partial differential equations - Calculus of Variations," *Math 220B Stanford - Course Notes*, 2004. available at J Levandovsky's stanford webpage.

[62] B. Yan, "Introduction to variational methods in partial differential equations and applications," *A summer course at Michigan State University (Math 890, Summer 2008)*, 2008.

[63] L. Pitaevskii and A. Rosch, "Breathing modes and hidden symmetry of trapped atoms in two dimensions," *Physical Review A*, vol. 55, no. 2, p. R853, 1997.

[64] R. D. Ruth, "A canonical integration technique," *IEEE Trans. Nucl. Sci.*, vol. 30, no. CERN-LEP-TH-83-14, pp. 2669–2671, 1983.

[65] R. I. McLachlan and P. Atela, "The accuracy of symplectic integrators," *Nonlinearity*, vol. 5, no. 2, p. 541, 1992.

[66] J. Candy and W. Rozmus, "A symplectic integration algorithm for separable Hamiltonian functions," *Journal of Computational Physics*, vol. 92, no. 1, pp. 230–256, 1991.

[67] H. Kinoshita, H. Yoshida, and H. Nakai, "Symplectic integrators and their application to dynamical astronomy," *Celestial Mechanics and Dynamical Astronomy*, vol. 50, pp. 59–71, 1991.

[68] C. J. Pethick and H. Smith, *Bose-Einstein condensation in dilute gases*. Cambridge university press, 2008.

[69] W. Kohn, "Cyclotron resonance and De Haas–Van Alphen oscillations of an interacting electron gas," *Physical Review*, vol. 123, no. 4, p. 1242, 1961.

[70] T. Bodurov, "Generalized Ehrenfest theorem for nonlinear Schrödinger equations," *International journal of theoretical physics*, vol. 37, no. 4, pp. 1299–1306, 1998.

[71] V. M. Perez-Garcia, H. Michinel, J. Cirac, M. Lewenstein, and P. Zoller, "Dynamics of Bose-Einstein condensates: Variational solutions of the

Gross-Pitaevskii equations," *Physical Review A*, vol. 56, no. 2, p. 1424, 1997.

[72] E. A. Cornell and C. E. Wieman, "Nobel Lecture: Bose-Einstein condensation in a dilute gas, the first 70 years and some recent experiments," *Reviews of Modern Physics*, vol. 74, no. 3, p. 875, 2002.

[73] A. L. Fetter and D. Rokhsar, "Excited states of a dilute Bose-Einstein condensate in a harmonic trap," *Physical Review A*, vol. 57, no. 2, p. 1191, 1998.

[74] M. Beau, J. Jaramillo, and A. Del Campo, "Scaling-up quantum heat engines efficiently via shortcuts to adiabaticity," *Entropy*, vol. 18, no. 5, p. 168, 2016.